STRUCTURAL PROPERTIES OF DEFECTED GRAPHENE NANORIBBONS UNDER TENSION: MOLECULAR-DYNAMICS SIMULATIONS

A THESIS SUBMITTED TO
THE GRADUATE SCHOOL OF NATURAL AND APPLIED SCIENCES
OF
MIDDLE EAST TECHNICAL UNIVERSITY

BY

BURCU TÜZÜN

IN PARTIAL FULFILLMENT OF THE REQUIREMENTS
FOR
THE DEGREE OF MASTER OF SCIENCE
IN
MICRO AND NANOTECHNOLOGY

JANUARY 2012

Approval of the thesis:

STRUCTURAL PROPERTIES OF DEFECTED GRAPHENE NANORIBBONS UNDER TENSION: MOLECULAR-DYNAMICS SIMULATIONS

submitted by **BURCU TÜZÜN** in partial fulfillment of the requirements for the degree of **Master of Science in Micro and Nanotechnology Department, Middle East Technical University** by,

Prof. Dr. Canan Özgen
Dean, Graduate School of **Natural and Applied Sciences** _____

Prof. Dr. Mürvet Volkan
Head of Department, **Micro and Nanotechnology** _____

Prof. Dr. Şakir Erkoç
Supervisor, **Physics Dept., METU** _____

Assoc. Prof. Dr. Almıla Güvenç Yazıcıoğlu
Co-supervisor, **Mechanical Engineering Dept., METU** _____

Examining Committee Members:

Prof. Dr. Lemi Türker
Chemistry Dept., METU _____

Prof. Dr. Şakir Erkoç
Physics Dept., METU _____

Assist. Prof. Dr. Tuba Okutucu Özyurt
Mechanical Engineering Dept., METU _____

Assoc. Prof. Dr. Cemil Yamalı
Mechanical Engineering Dept., METU _____

Assist. Prof. Dr. Emren Nalbant Esentürk
Chemistry Dept., METU _____

Date: **08.02.2012**

I hereby declare that all information in this document has been obtained and presented in accordance with academic rules and ethical conduct. I also declare that, as required by these rules and conduct, I have fully cited and referenced all material and results that are not original to this work.

Name, Last Name: BURCU TÜZÜN

Signature :

ABSTRACT

STRUCTURAL PROPERTIES OF DEFECTED GRAPHENE NANORIBBONS UNDER TENSION: MOLECULAR-DYNAMICS SIMULATIONS

Tüzün, Burcu
M.S., Department of Micro and Nanotechnology
Supervisor : Prof. Dr. Şakir Erkoç
Co-Supervisor : Assoc. Prof. Dr. Almıla Güvenç Yazıcıoğlu

January 2012, 64 pages

Structural properties of pristine and defected graphene nanoribbons have been investigated by stretching them under 5 percent and 10 percent uniaxial strain until fragmentation. The stretching process has been carried out by performing molecular dynamics simulations (MDS) at 1 K and 300 K to determine the temperature effect on the structure of the graphene nanoribbons. Results of the simulations indicated that temperature, edge shape of graphene nanoribbons and stretching speed have a considerable effect on structural properties, however they have a slight effect on the strain value. The maximum strain at which fracture occurs is found to be 46.41 percent whereas minimum strain value is calculated as 21.00 percent. On the other hand, the defect formation energy is strongly affected from temperature and edge shape of graphene nanoribbons. Stone-Wales formation energy is calculated as -1.60 eV at 1 K whereas -30.13 eV at 300 K for armchair graphene nanoribbon.

Keywords: graphene nanoribbons, defected graphene nanoribbons, molecular dynamics simulations

ÖZ

GERİLİM ALTINDAKİ HASARLI KARBON NANOŞERİTLERİN YAPILARININ İNCELENMESİ : MOLEKÜL-DİNAMİĞİ BENZETİŞİMLERİ

Tüzün, Burcu
Yüksek Lisans, Mikro ve Nanoteknoloji Bölümü
Tez Yöneticisi : Prof. Dr. Şakir Erkoç
Ortak Tez Yöneticisi : Doç. Dr. Almıla Güvenç Yazıcıoğlu

Ocak 2012, 64 sayfa

Hasarlı ve hasarsız grafen nanoşeritlerin yapısal özellikleri, bu yapıların bozulma noktasına kadar yüzde 5 ve yüzde 10 oranlarında tekeksenli gerdirilmesiyle incelenmiştir. Molekül dinamiği benzetişimi (MDB) ile 1 K sıcaklığında gerçekleştirilen uzatma işlemi, sıcaklığın grafen nanoşeridin yapısı üzerindeki etkisini gözlemleyebilmek için 300 K sıcaklığında tekrarlanmıştır. Benzetişim sonuçları göstermiştir ki; sıcaklık, uzama hızı ve nanoşeridin köşe yapısı şekil özellikleri üzerinde önemli ölçüde bir etkiye sahipken; gerinim değerini çok az etkilemiştir. Kırılmanın gerçekleştiği en yüksek gerinim değeri yüzde 46.41 olarak tespit edilirken, en düşük gerinim değeri ise yüzde 21.00 olarak hesaplanmıştır. Diğer taraftan hasarların oluşum enerjisi üzerinde sıcaklığın çok önemli bir etkisi vardır. Koltuk köşe yapılı nanoşeritlerdeki Stone-Wales hasarlarının oluşum enerjisi 1 K sıcaklıkta -1.6 eV, 300 K sıcaklıkta ise -30.13 eV olarak tespit edilmiştir.

Anahtar Kelimeler: grafen nanoşeritler, hasarlı grafen nanoşeritler, molekül dinamiği benzetişimleri

To my dear fiance Akif, my mother and sister

ACKNOWLEDGMENTS

I am deeply grateful to my supervisor Prof. Dr. Şakir Erkoç for his valuable guidance, encouragement and technical support throughout this thesis work. I am thankful to my cosupervisor Assoc. Dr. Almıla Güvenç Yazıcıoğlu for her constructive comments.

I would also like to sincerely thank to Akif, my dear fiance; my mother and sister for their patience, support and love which make life worth to live for me.

TABLE OF CONTENTS

LIST OF TABLES

TABLES

LIST OF FIGURES

FIGURES

CHAPTER 1

INTRODUCTION

In this section, a general information about graphene and graphene nanoribbons is presented. Firstly, graphene is introduced since it is the building block of graphene nanoribbons. Then, graphene nanoribbons and their properties are investigated.

1.1 Graphene

Carbon is an important element at nanoscale because of its capability of forming different low dimensional structures such as graphene (2D), carbon nanotubes (CNT) (1D), and fullerenes (0D) which have superior physical properties [1].

A graphene layer is composed of sp^2 hybridized carbon atoms [2] playing a role in mechanical stability of graphene layer. P orbitals perpendicular to molecular plane hybridize to form conduction and valance bands [3]. Electrical properties of graphene monolayer is affected by this band structure [4]. The bond structure of graphene layer is depicted in Figure 1.1.

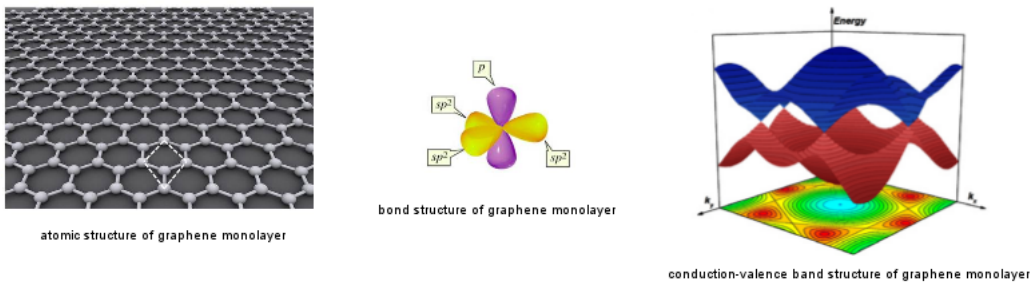

Figure 1.1: Atomic, bond and band structures of graphene monolayer.

Edge shape of graphene layer manipulates its properties [5]. Chiral vector (n,m) describes both edge shape of graphene [5] and direction of wrapping graphene sheet to form carbon nanotubes [6]. Chirality of graphene layer depicted by chiral vector (n,m) can be explained by using Figure 1.2. In this figure, a_1 and a_2 are the lattice vectors. The chiral vector is presented as linear combination of these lattice vector such that (na_1 + ma_2). The coefficients n and m indicates the number of lattice vectors along graphene sheet. By changing these coefficients, different graphene types can be obtained named as chiral graphene. Zigzag graphene sheet is obtained by taking m to be zero. If m equals n, armchair graphene is obtained [6].

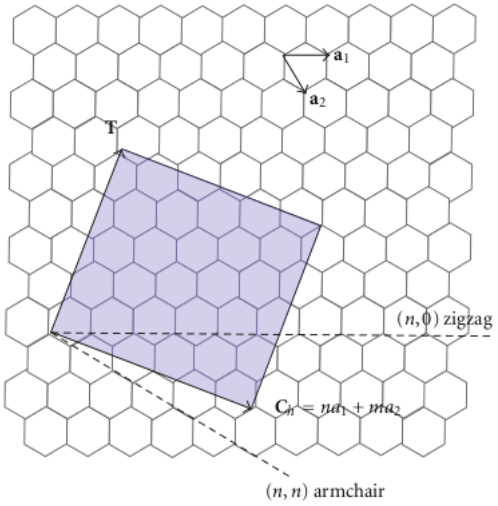

Figure 1.2: Chirality of graphene sheet and chiral vector [7].

Until 2004, it was thought that films with thickness at nanometer scale are thermodynamically unstable. In 2004, Novoselov and coworkers [8] were able to prepare single layer graphene. Since the isolation of either single or a few atom thickness graphene layers, applications of graphene arouse interest among scientists because of its novel properties [9]. 2D graphene layer can be considered as a building block of different carbon structures. For example, by rolling the graphene layer and in turn, creating carbon nanotubes (CNT) [1], by wrapping graphene and forming spherical buckyballs and by putting them one after the other, graphite can be obtained [9]. The popularity of 2D graphene layer emanates from its unique electrical properties, on which large number of studies have been reported in the literature [10, 11, 12, 13].

1.1.1 Electrical Properties of Graphene

When the band structure of single layer graphene is investigated, it is observed that conduction and valance band are touching at one point called Dirac point [11]. Therefore, graphene is known as zero-gap semiconductor. By application of electric field, electron carrier density or hole carrier density in graphene can be controlled. Therefore, graphene based transistor is termed as ambipolar field effect transistor (FET). As illustrated in Figure 1.3 applying negative voltage introduces positive hole carriers, however applying positive voltage induces negative electron carriers [14]. In other words, p-type or n-type FET can be obtained just by changing voltage polarity. The conductance increases with applying non-zero voltage, but it is minimum at zero voltage. This property makes graphene attractive material for electronic device application. It is reported in [15] that charge carriers in monolayer graphene behave like a massless Dirac fermions with 10^{-6} m/s velocity. The highest value of the carrier mobility for graphene monolayer is reported as $2{\times}10^5$ $cm^2V^{-1}s^{-1}$ in the literature [16] .

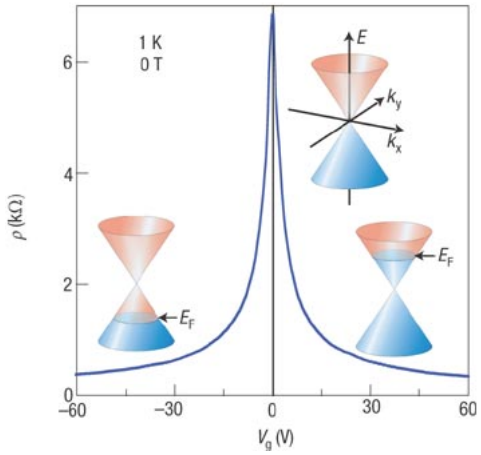

Figure 1.3: Band structure and ambipolar field effect in single layer graphene [14]

1.1.2 Mechanical Properties of Graphene

The research carried on mechanical properties of graphene is less than the research carried on electrical and optical properties of graphene [3]. Although the popularity of graphene comes from its unique and strange electrical properties, graphene has also remarkable mechanical properties [17]. If graphene is used in micro and nano scale machines such as nanogears,

membranes, accelerometer, cantilevers, actuators; then the mechanical properties of graphene become important as much as its electrical properties. The breaking strength measured by atomic force microscope of defect-free monolayer graphene sheet is reported as 42 N/m by Lee et al. in [18]. The experiment carried by Bunch et al. [19] indicated some important mechanical properties of one atom thickness graphene membrane. In this experiment, one side of the graphene membrane with one atom thickness was exposed to atmospheric pressure while the pressure on the other side was changed by using helium gas. Since graphene membrane is impermeable to the helium gas, the pressure can be controlled by changing the amount of helium. The deflection of the graphene membrane arising from the pressure differences has been used to calculates the mechanical properties. The elastic constant and stiffness (Young's modulus) of graphene membrane have been reported in [19] as nearly 390 N/m and nearly 1 TPa, respectively. Graphene membrane is also appropriate candidate to be used in resonators due to its high Young's modulus and low mass. In the resonators, the graphene membrane vibrates as a result of applied force. The resonant frequency (f_0) of 15 nm thick graphene membrane is detected as 42 MHz with 210 quality factor, whereas the resonant frequency of one atom thick graphene layer is 70.5 MHz with 78 quality factor [20]. Quality factor is a dimensionless parameter and mathematically defined as fraction of resonant frequency (f) and bandwidth (Δ f), namely $\frac{f}{\Delta f}$ [21].

1.1.3 Commercial Applications of Graphene

The importance of graphene comes from its large application areas. For example, graphene is an excellent choice for fabrication of ultrafast transistors because of its ability of outstanding electron transport at room temperature. Graphene is also preferred in the biosensors and chemical sensors because of its low capacitance resulting in low signal to noise ratio, and rapid electron transfer resulting in accurate and selective detection of biomolecules [22]. Some robust polymer composites (poly-vinyl-alcohol/graphene), high electrical conducting (polystyrene/graphene), high thermal conducting polymers (epoxy resins/graphene composites) and more thermally stable polymers can be produced by using graphene as fillers during fabrication [23]. Moreover, using graphene instead of carbon nanotubes (CNT) decrease production costs and difficulties that stem from reliability problems due to chirality of CNT [23, 24]. Graphene is suitable to be used as electrode material in capacitors [25] and lithium-ion batteries [26] because its wide surface area (2630 m^2g^{-1}), high electrical conductivity (64 mS

cm^{-1}), stability over vast range of temperature and high electron mobility (2×10^5 $cm^2V^{-1}s^{-1}$ at electron densities of 2×10^{11} cm^{-2} for 150 nm graphene nano sheet above Si/SiO_2 gate) make graphene a good choice for energy storage [9]. Apart from these, graphene is preferred also in energy generation devices due to its electro-catalytic activity, enzymatic binding capacity, unique electrical properties and low production cost. It can also be possible to detect the bio-molecules, drugs, heavy metals or catalytic surfaces by the help of the presence of the defects or dopants. However, having knowledge on defects is crucial to control chemical, electronic, mechanical and magnetic properties of graphene [1].

1.2 Defects

It is obvious that the strength of graphene depends on the number and types of defects and also edge termination. There are different types of defects such as doping-induced defects caused by substitution of non-carbon atoms in graphene sheet, structural defects, grain boundaries defect, bond rotation defect and non-sp^2 carbon defects resulted by dangling bonds [1]. Apart from mechanical strength, defects also play a crucial role in physicochemical properties, chemical activity, structure, topology, cavity [1], optical, electronic and thermal properties [2]. Moreover, conductance and ductility of graphene based devices are controlled by defect characteristic of graphene. In other words, structural defects in graphene layer that appear during processing or growth have a great effect on the performance of the graphene based devices. Because of these structural defects, graphene based devices may lose their functional quantity or gain superior or new functionalities depending on type, location or size of the defects. For example, graphene is generally used to enhance and improve the strength of composites. However, research carried out by Bartolucci and coworkers [27] showed that the strength of graphene-aluminum composites is lower than that of pure aluminum and aluminum-carbon nanotubes composites. Lower mechanical strength is explained by defects which become reaction sites with aluminum and result in significant amount of aluminum carbide(Al_4C_3) as points of weakness [27]. In some cases, defected graphene is favorable such as earth metal dispersion on graphene layer and hydrogen adsorption. Hydrogen has very limited interaction with graphene [24] which results in using metals such as lithium or palladium to adsorb or decompose hydrogen for sensing [24, 28]. Metal atoms such as lithium binding on graphene vacancies with energy higher than cohesive and cluster forming energy are the active side

for hydrogen adsorption [28]. The structure is also affected from defect due to different hybridization ability of carbon atoms which cause different stable structures such as carbyne or graphite. Moreover, the flat structure of graphene layer may be deformed due to non-hexagonal carbon arrangements when polygons can not satisfy symmetry rules. This local curvature allow reactivity and adsorption [2].

1.3 Graphene Nanoribbons

There are some limitations in the applications of graphene in (FET), since graphene is a zero band gap semiconductor. This problem has been solved by using graphene nanoribbon (GNR) which can be synthesized by finite termination of graphene sheet. A non-zero band gap originated from quantum confinement varies from 200 meV to 0.4 eV depending on the width of the nanoribbon [29]. In the present study, two types of GNRs are examined, which are classified according to their edge shape as zigzag GNR and armchair GNR.

1.3.1 Electrical Properties of GNRs

GNRs show metallic or semiconducting behavior depending on ribbon width and on edge shape such as zigzag edge shape or armchair edge shape [30]. A sharp peak in the density of states (DOS) at the Fermi level is obtained for zigzag GNRs because of localized edge states [30]. This is also the reason of magnetic behavior of zigzag GNRs [31]. Armchair GNRs possess either metallic or semiconducting behavior depending on ribbon widths. On the other hand, zigzag GNRs have always metallic properties, whatever the ribbon widths might be. The research carried out by Son et al. [31] reported that both armchair and zigzag graphene nanoribbons passivated with hydrogen have non zero and direct band gap. The genesis of band gaps are explained by quantum confinement for armchair GNR. The band gaps of zigzag GNR are based on staggered sublattice potential because of spin ordered states at the edges since opposite spin states are localized on opposite edges. The band gaps decrease with increasing ribbon width for both zigzag and armchair GNRs. Moreover, edge effect has important effect on band gaps for both zigzag and armchair GNR.

The conductance of GNR decreases by several Fermi energies in the first subband due to

vacancy. The suppression of conductance arises from the electron localization near vacancy. This suppression of conductance can be eliminated by introducing a perpendicular magnetic field with sufficient strength which removes the localization. The defects near the center have larger influence on the reduction of conductance than that of the defects near the edge [32].

1.3.2 Mechanical Properties of GNRs

The structure and size of the GNR have important influence on the mechanical properties. Some important and basic mechanical properties such as Young's modulus have been reported by several researches. However, there is limited information about defect's evolution and its effect on the mechanical properties of the GNR in the literature [33]. The Young's modulus of the GNR is reported to vary from 0.7 TPa to 7 TPa. The variation in the stiffness originates from the method used to investigate the mechanical properties of GNR. The Young's modulus of GNR is reported nearly 0.7 TPa according to atomistic simulations method [35]. However, the experimental method carried by Hod and Scuseria [36] gives 7 TPa Young's modulus which is seven times higher than that of monolayer graphene sheet. The slight influence of the edge shape of the GNR on the mechanical properties can be seen from Table 1.1 [37].

Table 1.1: Fundamental mechanical properties of graphene nanoribbon at 300 K [37]

GNR	**Young's Modulus (GPa)**	**Yielding Strength (GPa)**	**Breaking Strain**
armchair GNR	720	83	0.16
chiral GNR	714	85	0.175
zigzag GNR	710	98	0.24

Figure 1.4 and Figure 1.5 present the result of the research carried out by Georgantzinos et al. in [33]. In this work, width and length of the ribbons are taken as parameters, and both zigzag and armchair graphene nanoribbons have been investigated. As depicted in Figure 1.4, the Young's modulus of the pristine armchair graphene nanoribbon is a bit higher than that of the pristine zigzag graphene nanoribbon. If the length of the ribbons is taken constant, the Young's modulus of armchair GNRs decreases with increasing width. On the other hand, Young's modulus of the zigzag GNR increases with increasing width. If the width of the ribbons is taken constant, the Young's modulus of zigzag GNR changes drastically, while the Young modulus of the armchair GNR is influenced slightly from the change in the length.

For both ribbons, the maximum Young's modulus is obtained at minimum length. The strain value, at which the ribbons are broken, is shown in Figure 1.5. The strain values of armchair GNR are higher than that of zigzag GNRs.

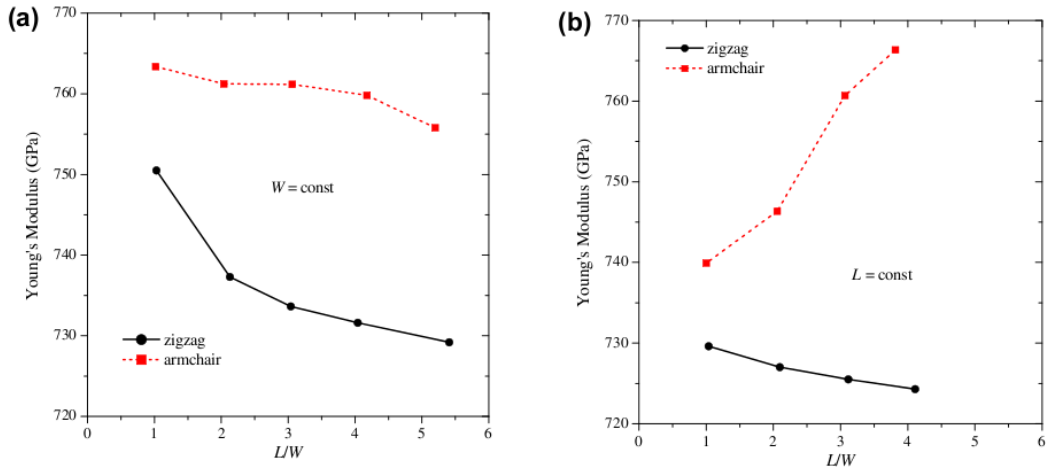

Figure 1.4: Young modulus of the GNRs for constant width (a) and for constant length (b) with respect to aspect ratio(L/W) [33]

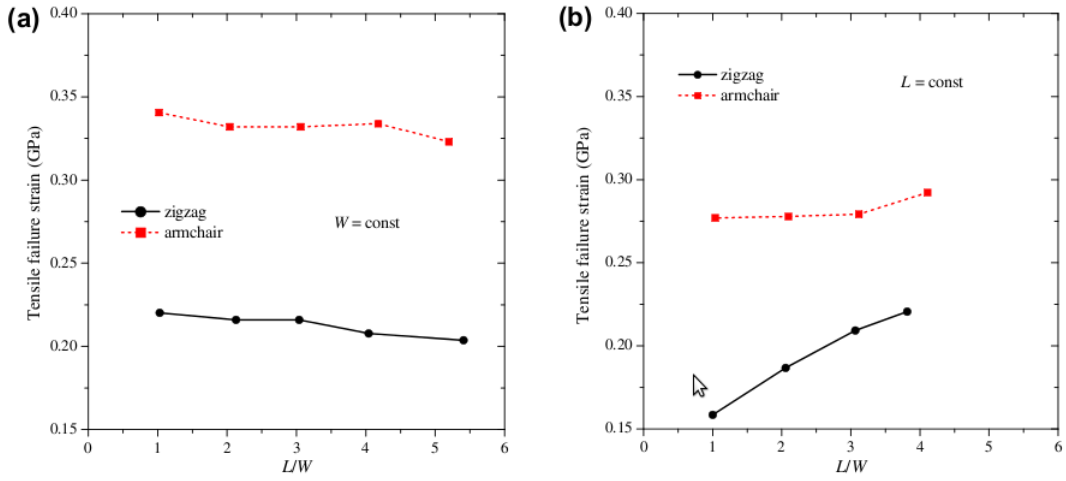

Figure 1.5: The strain values of GNRs for constant width (a) and for constant length (b) with respect to aspect ratio(L/W) [33]

1.4 Outline of the Thesis

In this work, 2D graphene nanoribbon in two different structures which are zigzag and armchair models are studied and presented in Figure 1.6. The main motivation of this work is

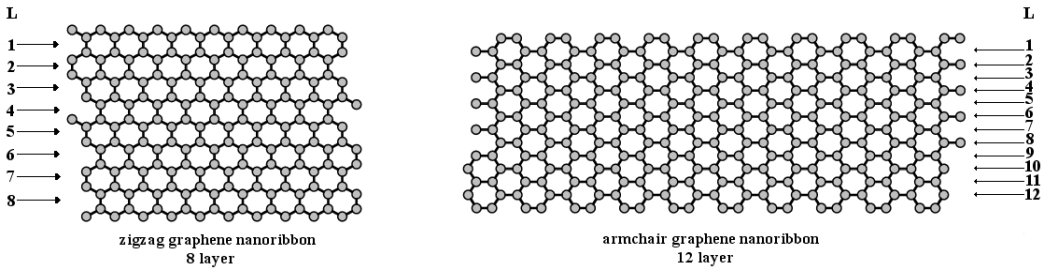

Figure 1.6: Zigzag and armchair graphene nanoribbon models

the limited information on the mechanical properties of defected GNRs. Figure 1.7 presents the structural defects considered in this work, which are monovacancy, divacancy and Stone-Wales defects. The other property of defects is mobility. Defects are not stationary, they have a certain mobility parallel to the graphene ribbons plane. The characteristic of migration depends on types of defects and temperature [2]. In the present study, the migration of defects are also observed.

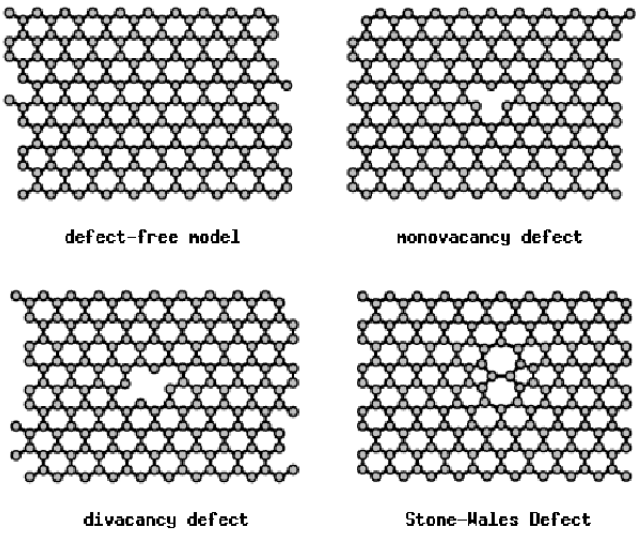

Figure 1.7: Types of defects in graphene nanoribbons

The width of the armchair and zigzag GNRs is tried to be kept close to each other by taking

the models at different layers in order to understand the chirality effect better. For example, the width of the zigzag model with 8 layers is close to the width of the armchair model with 12 layers as seen from Figure 1.6. In the present thesis, 8 layer zigzag GNR with 24.60 Å initial length and 12 layer armchair GNR with 42.60 Å initial length are compared to investigate chirality effect on the strength. There is no particular reason choosing these lengths. Effects of the difference in the initial length are dismissed by applying periodic boundary condition. In order to eliminate the differences in the initial length, strain values are compared instead of final length at which fracture occurs.

Previously, the MD program used in the present study was tested by using same potential energy function [34]. Before the stretching process, an appropriate working cell has been generated by defining the initial position of carbon atoms. Periodic boundary conditions are applied in the direction in which the stretching process is carried out. MD relaxation is carried out till the total energy of the system is constant with respect to time. 10^5 MD steps were enough to reach equilibrium for the models considered in this study. After the system reaches equilibrium the stretching process is begun by extending the geometry by 5 percent. At each stretching process, the system was relaxed till the equilibrium was reached. Stretching and relaxation processes have been continued till some of the bond are broken and the nanoribbon starts to fragment. The method used in this work is explained in detail in Chapter 2.

CHAPTER 2

THEORETICAL BACKGROUND

This section is divided into two parts. In the first part, the method followed during the research is introduced with general view. In the second part, some details of the method are given.

2.1 Method of Calculations

MDS method known from 1960 is a very powerful technique to study the materials at nanoscale because lots of interactions are taken into account by MDS which can not be ignored at nanoscale as done at macroscale [38].

In this work, classical MDS was performed in a canonical ensemble system to investigate the structural properties of graphene nanoribbons. According to canonical ensemble, the temperature is taken as constant via Hoover thermostat. Due to periodic boundary conditions, the number of particles is also constant. Verlet Algorithm is used for time integration and velocity calculations. The interaction between particles are calculated according to Tersoff potential energy functions in which the strength of the bonds between two atoms are not constant and the parameters are different for each elements [39].

MDS is carried out at 1 and 300 K in order to understand the effect of temperature on the defect mobility and fragmentation mechanism. Before the stretching process, an appropriate cell has been generated by defining the initial position of carbon atoms. When total energy is constant with respect to iteration number, it is assumed that the system reaches equilibrium. 10^5 MD steps were enough to reach equilibrium for the models considered in the present

study. The flowchart of the MD program is presented in Appendix C.

After the system reaches the equilibrium, the stretching process is begun by extending the geometry by 5 or 10 percent. At each stretching process, the system was relaxed until reaching equilibrium. Periodic boundary conditions are applied in the direction which the stretching process is carried out. When the geometry breaks down, the process reaches the end, and the change in stretching energy is available.

In this work, graphene naoribbon with two different chiralities (zigzag and armchair) and with different layer (the width of the nanoribbon) have been studied. The width of the armchair and zigzag graphene nanoribbons is tried to be kept close to each other by taking the models at different layers in order to understand the chirality effect better. For example, the width of the zigzag model with 8 layers is close to the width of the armchair model with 12 layers as seen from Figure 1.6. In the present work, 8 layer zigzag GNR with 24.60 Å initial length and 12 layer armchair GNR with 42.60 Å initial length were compared to investigate chirality effect on the strength. The stretching process has been carried only for 12 layer armchair GNR and 8 layer zigzag GNR, because the defects can be set in the midst properly for these models. In order to eliminate the differences in the initial length, strain values were compared instead of final length at which fracture occurs.

2.2 Simulations in Detail

2.2.1 Molecular Dynamics Simulations

MD introduced firstly by Alder and Wainright [40] is a method used to determine the physical quantities over a restricted set of states [41]. In addition, MD can be used to study non-equilibrium system, dynamic phenomena (transport of heat or charge), kinetic phenomena or relaxation of system far from equilibrium [41, 42]. This is the great advantage of the MD method over Monte Carlo method [41].

Molecular dynamics simulation is based on numerical and step by step solution of classical

equation of motion which is given in Equation 2.1 for simple atomic system.

$$\frac{\partial^2 x_i}{\partial t^2} = -\frac{1}{m_i}\nabla_i \varphi; \qquad i = 1, 2, ..., 3N \tag{2.1}$$

To calculate equation of motion, it is needed to be able to calculate the forces (φ) acting on atoms which is performed by potential energy function(PEF) and the initial position of the atoms must be known. Periodic boundary condition is applied to constrain the volume and number of atoms.

Usually, classical MDS was performed in a microcanonical ensemble system in which energy, momentum, particle number and volume are taken as constant [41]. However, in experimental situation total energy of the system does not taken as control variable. By some modification, MD can be used for a system in which temperature or pressure is kept constant called as canonical ensemble. The MD method based on canonical ensemble, which is closest to the experimental systems, was introduced by Andersen in 1980 [43].

2.2.2 Verlet Algorithm

The differential function indicated in Eq 2.1 has been calculated by Verlet Algorithm [44]. The positions (r(t)) at time step t, and previous time step are used to calculate new position. The following equations have been given to summarize the algorithm [45]. Taylor series expansion for position is given in Eq 2.2.

$$r(t + \delta t) = r(t) + \delta t\frac{\partial r}{\partial t} + \frac{1}{2}\delta t^2\frac{\partial^2 r}{\partial t^2} + \frac{1}{6}\delta t^3\frac{\partial^3 r}{\partial t^3} + ... \tag{2.2}$$

It is obvious that the first derivative of the position with respect to time is velocity (v), and the second derivative of position with respect to time is acceleration (a)

$$r(t + \delta t) = r(t) + \delta t v(t) + \frac{1}{2}\delta t^2 a(t) + \frac{1}{6}\delta t^3\frac{\partial^3 r}{\partial t^3} \tag{2.3}$$

$$r(t - \delta t) = r(t) - \delta t v(t) + \frac{1}{2}\delta t^2 a(t) - \frac{1}{6}\delta t^3\frac{\partial^3 r}{\partial t^3} \tag{2.4}$$

Adding the Equation 2.3 and the Equation 2.4 gives;

$$r(t + \delta t) = 2r(t) - r(t - \delta t) + \delta t^2 a(t) \tag{2.5}$$

The velocities which is used for kinetic energy calculation can be calculates as indicated in Equation 2.6.

$$v(t) = \frac{r(t + \delta t) - r(t - \delta t)}{2\delta t} \tag{2.6}$$

2.2.3 Tersoff Potential

According to the Tersoff Potential Function approach, the bond strength depends on local environment; in other words the atoms with many neighbor has weaker bond than that of atoms with few neighbors. Using quantum-mechanical calculation to determine the energy of atoms as a function of atomic coordinates is not feasible for large systems due to complexity of quantum-mechanical calculations. One of the possible solution is an empirical interatomic potential since it is easy to calculate and also provides accurate results. In the present work, Tersoff Potential Energy Function has been used which is proposed by Tersoff firstly for silicon [46] and then it was calibrated for carbon [39]. The following equations have been given to summarize the Tersoff PEF to calculate the interaction between particles. The energy of N-interacting particles can be calculated as indicated in Equation 2.7.

$$E = \Sigma_i V_1(r_i) + \Sigma_{i<j} V_2(r_i, r_j) + \Sigma_{i<j<k} V_3(r_i, r_j, r_k) + ... \tag{2.7}$$

Where r_n is the position of the nth particle and V_m is m-body potential (V_2 is two-body potential and V_3 is three-body potential). V_1 is an external potential. The potential energy function showing the interaction of particle begin by the second term. The interatomic potential was taken as indicated in Equation 2.8 by Tersoff, in order to implicit the geometry dependency of bond energy.

$$E = \Sigma_i E_i = \frac{1}{2} \Sigma_{i \neq j} V_{ij} \tag{2.8}$$

where V_{ij} is defined by;

$$V_{ij} = f_c(r_{ij})[a_{ij} f_R(r_{ij}) + b_{ij} f_A(r_{ij})] \tag{2.9}$$

r_{ij} represents the distance between atom i and atom j. f_A (2.11) and f_R (2.10) is used to indicate attractive pair potential function and repulsive pair potential function, respectively. f_c represents smooth cutoff function.

$$f_R = Aexp(-\lambda_1 r) \tag{2.10}$$

$$f_A = -Bexp(-\lambda_2 r) \tag{2.11}$$

$$f_c = \begin{cases} 1 & \text{if } r_{ij} < R - D \\ 0.5 - 0.5[sin(\frac{\pi(r_{ij})\pi - R}{2D})] & \text{if } R - D < r_{ij} < R + D \\ 0 & \text{if } r_{ij} > R + D \end{cases}$$

The other parameters are taken in the following form as indicated in Equations 2.12, 2.13, 2.14, 2.15, 2.16.

$$b_{ij} = [1 + \beta^n \zeta_{ij}^n]^{-\frac{1}{2n}} \tag{2.12}$$

$$\zeta_{ij} = \Sigma_{k \neq i,j} f_c(r_{ik} g(\Theta_{ijk}) exp[\lambda_3^3 (r_{i,j} - r_{ik})^3] \tag{2.13}$$

$$g(\Theta_{ijk}) = 1 + \frac{c^2}{d^2} - \frac{c^2}{d^2 + (h - cos\Theta_{ijk})^2} \tag{2.14}$$

where Θ_{ijk} is bond angle between bonds ij and ik.

$$a_{ij} = (1 + \alpha^n \eta_{ij}^n)^{-\frac{1}{2n}} \tag{2.15}$$

$$\eta_{ij} = \Sigma_{k \neq i,j} f_c(r_{ij}) exp[\lambda_3^3 (r_{ij} - r_{ik})^3] \tag{2.16}$$

The constants for carbon atoms can be obtained from Reference [39] and are indicated in Table 2.1.

Table 2.1: Parameters for Tersoff potential for carbon atoms

A	1393.6 eV
B	346.74 eV
λ_1	3.4879 Å
λ_2	2.2119 Å
β	1.5723×10^{-7}
n	0.72751
c	38049
d	4.3484
h	-0.57058
R	1.95 Å
D	0.15 Å
α	0
λ_3	0

2.2.4 Periodic Boundary Condition

In the present study, periodic boundary conditions (PBC) has been applied which is powerful method to simulate homogeneous systems. According to PBC, the system is constructed by

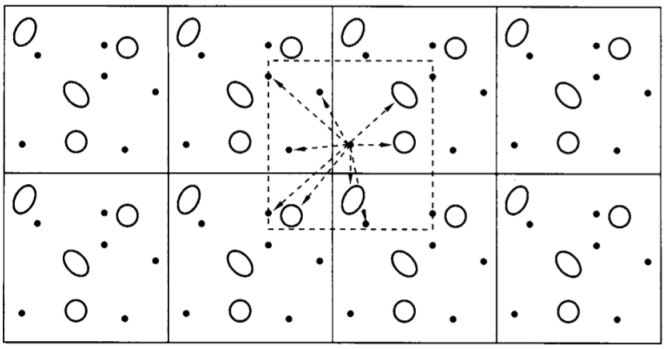

Figure 2.1: Two-dimensional representation of periodic boundary conditions [47]

replication of primitive cell to give infinite periodic lattice as indicated in Figure 2.1 [47]. PBCs can be implemented via nearest image convention (NIC) [48]. According to this approach, if the distance between two particles i and j larger than $\frac{L}{2}$, then the interaction between i and j has been neglected. Instead of j, j′ which is periodic image of j at the coordinates r_{ij}−L interacts with i, and that interaction potential has been taken [49]. NIC has been carried by the transformation represent in Equation (2.17)

$$\begin{aligned} if \quad & r_{ij_\alpha} > L/2 \quad r_{ij_\alpha} \longleftarrow r_{ij_\alpha} - L \\ if \quad & r_{ij_\alpha} < L/2 \quad r_{ij_\alpha} \longleftarrow r_{ij_\alpha} + L \end{aligned} \tag{2.17}$$

where α can be x, y or z. By using periodic boundary conditions (PBC), the number of particles are kept constant in the system. Therefore, the particle which leaves the boundary during simulation re-enters on the opposite face [34]. In addition, the surface effect can be eliminated, and the system can be made pseudo-infinite by the application of periodic boundary condition [42].

2.2.5 Nose-Hoover Algorithm

As a summary in MDS used in the present work canonical ensemble has been used. This is known also (NVT), since number of particles(N), volume of the system(V) and temperature(T) are kept constant. The number of particles and the volume of the system are kept constant by periodic boundary implication. The temperature is kept constant by using Nose-Hoover thermostat which was proposed by Nose [50] and developed by Hoover [51].

The implementation of Nose-Hoover equations of motion into MD program can not be done directly. Firstly, the Verlet velocity algorithm for standard micro-canonical system is used to calculate initial velocity and position as indicated in Equation 2.18. The energy of the system changes during the simulation. The temperature of the system is affected from this change. The change in the temperature is calibrated by re-scaling the velocity and position according to Nose-Hoover approach.

$$\begin{aligned} r(t+\Delta t) &= r(t) + v(t)\Delta t + f(t)\frac{(\Delta t)^2}{2m} \\ v(t+\Delta t) &= v(t) + \frac{f(t+\Delta t) + f(t)}{2m}\Delta t \end{aligned} \tag{2.18}$$

The obtained velocity and position according to Nose-Hoover equation of motion are given in the Equation 2.19 which can be solved by iteration.

$$\begin{aligned} r_i(t+\Delta t) &= r_i(t) + v_i(t)\Delta t + [\frac{f_i(t)}{m_i} - \xi(t)v_i(t)]\frac{(\Delta t)^2}{2} \\ v_i(t+\Delta t) &= v_i(t) + [\frac{f_i(t+\Delta t)}{m_i} - \xi(t+\Delta t)v_i(t+\Delta t) + \frac{f_i(t)}{m_i} - \xi(t)v_i(t)]\frac{\Delta t}{2} \end{aligned} \tag{2.19}$$

2.2.6 Modeling Uniaxial Stretching

Uniaxial stretching is applied on the models by multiplying the length of the model by 1.05 (for slow stretching) or by 1.1 (for fast stretching). As depicted in Figure 2.2, model is stretched only in x direction by incrementation periodic boundary length and rearranging x coordinates of atoms. Amount of increase in length is presented as ΔL. ΔL equals to 0.05× L_i for slow stretching and 0.1× L_i for fast stretching, where L_i is previous length of ribbon.

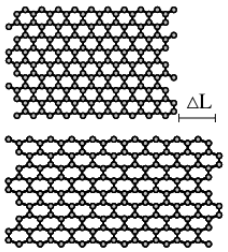

Figure 2.2: Schematic presentation of the stretching process.

CHAPTER 3

RESULTS AND DISCUSSIONS

3.1 Zigzag GNRs with the Set of diverse Defects

In this work, divacancy, monovacancy and Stone-Wales defects have been examined. In order to clearly understand the effects of these defects on the structure, shape and location of the defects were also changed. Figure 3.1 presents the set of diverse defects examined in zigzag GNRs. Defect formation energies, strain values and strain energies are calculated by using total energies and lengths of the structures. The raw data obtained at each stretching step for pristine and defected zigzag GNRs is given in Appendix A.

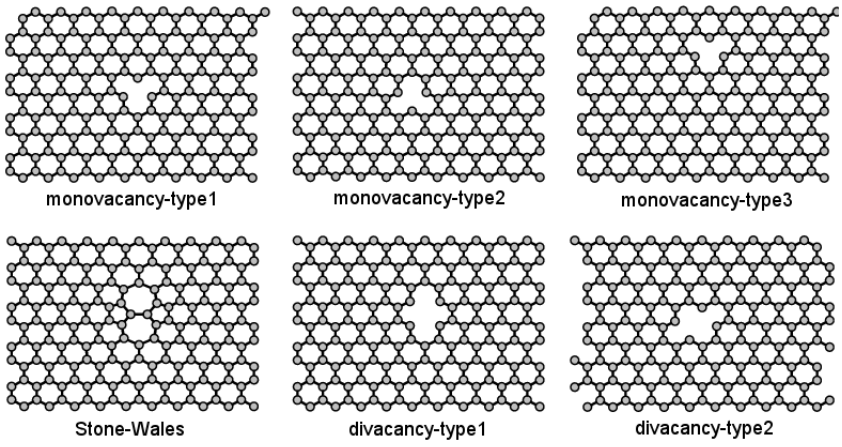

Figure 3.1: A diverse set of defects in zigzag GNRs

The formation energies give information about the tendency of a defect formation on GNRs. DFT calculation results for defect formation energies for CNTs and graphene sheets are avail-

able in the literature [52, 53, 54]. However, these quantities are not available for pristine or defected GNRs.

The calculated formation energies E_{fe} of the monovacancy, divacancy and Stone-Wales defects for zigzag GNR are given in Table 3.1. In this study, defect formation energy E_{fe} is defined to be the differences between the total energies of the pristine and defected GNR with the condition that they have the same width, length and edge form, namely, $E_{fe} = E_{Tp} - E_{Td}$. E_{Tp} and E_{Td} are the total energies of pristine and defected GNRs, respectively. As depicted in Table 3.1, all defect formation energies are negative and different from each other. Although both divacancy-type1 and divacancy-type2 have the same number of missing atoms resulting in defects, defect formation energies are different from each other. The same conclusion is valid for monovacancy defects, as well.

Table 3.1: Defect formation energies (E_{fe}, in eV) of zigzag 8 layer GNRs

Defect type	**E$_{fe}$ (at 1 K)**	**E$_{fe}$ (at 300 K)**
monovacancy-type1	-21.47	-32.58
monovacancy-type2	-26.62	-26.68
monovacancy-type3	-16.25	-25.57
Stone-Wales	-26.94	-50.59
divacancy-type1	-31.87	-44.00
divacancy-type2	-23.41	-28.35

Previously, E_{fe} is defined as the difference between total energy of pristine and defected GNR. It can be drawn out that defected GNR whose energy is close to the energy of pristine GNR, is more likely to form. As presented in Table 3.1, due to negative E_{fe} values, defected model with highest defect formation energy is actually the one closest to the pristine model in terms of total energy. In this case, at 1 K for zigzag GNRs, the defect type can be sorted in descending order in terms of tendency as follows; monovacancy-type3, monovacancy-type1, divacancy-type2, monovacancy-type2, Stone-Wales, divacancy-type1.

Defect formation energies decrease with increasing temperature. The amount of decrease is different for each model. E_{fe} at 300 K for zigzag GNR is different than that of the one at 1 K which also affects the order of tendency among defects. At 300 K for zigzag GNR, the

defect type can be sorted in descending order in terms of tendency as follows; monovacancy-type3, monovacancy-type2, divacancy-type2, monovacancy-type1, divacancy-type1, Stone-Wales. At 300 K, the defect formation energy of monovacancy-type2 does not change, unexpectedly.

The defect formation energies of monovacancy-type1 and monovacancy-type3 decrease by 51.75 percent and 57.35 percent, respectively due to raise in temperature. The change in defect formation energies is calculated as $(E_{fe_{300K}} - E_{fe_{1K}})/E_{fe_{1K}} \times 100$ in percentage, where $E_{fe_{300K}}$ and $E_{fe_{1K}}$ are defect formation energies at 300 K and 1 K, respectively. The defect formation energy of divacancy-type1 decreases by 38.1 percent whereas E_{fe} of divacancy-type2 decreases by 21.1 percent. Hence, the E_{fe} of defects are affected from both temperature and the shape of the defects. Moreover, it might be different despite the equality of the number of missing atoms resulting in defects. At 300 K, E_{fe} of Stone-Wales (-50.59 eV) drastically decreases by 87.79 percent and becomes the defect that most likely to form at room temperature. To conclude, monovacancy-type3 defect is the most likely model to form among the others at both 1 and 300 K. Defect formation energies are not only affected from temperature but also from chirality which is discussed in section 3.2.

The strain values calculated at fragmentation point for zigzag GNRs are listed in Table 3.2. Strain is defined to be the difference in length in percentage, namely, strain= $100 \times \frac{L_i - L_0}{L_0}$. L_i is the length of the nanoribbon at the i^{th} stretching step and L_0 is the initial length. The maximum strain value is obtained as 46.41 for pristine, monovacancy-type3 and Stone-Wales zigzag GNRs at 1 K under fast stretching process. The minimum strain value is obtained as 21.00 for monovacancy-type1, monovacancy-type2 and Stone-Wales defected zigzag GNRs at 300 K under fast stretching process. As shown in Table 3.2 strain values are affected from temperature. For example, for zigzag GNRs strain values obtained at 300 K are smaller than those at 1K. However, the results are not sufficient to compare the strain values of the different defects. We note that the strain values for different defect models are the same; this shows that different defected structures can show similar characteristics under similar conditions.

The results of the zigzag GNR stretching simulations are presented in Figures 3.2- 3.8. These

Table 3.2: Calculated failure strain values for pristine and defected zigzag GNRs

Graphene model and Defect type	**Temperature (K)**	**Stretching Type**	**Strain**
zz8L-pristine	1	slow	40.71
zz8L-pristine	1	fast	46.41
zz8L-pristine	300	slow	27.63
zz8L-pristine	300	fast	33.10
zz8L-monovacancy-type1	1	slow	34.01
zz8L-monovacancy-type1	1	fast	33.10
zz8L-monovacancy-type1	300	slow	21.55
zz8L-monovacancy-type1	300	fast	21.00
zz8L-monovacancy-type2	1	slow	34.01
zz8L-monovacancy-type2	1	fast	33.10
zz8L-monovacancy-type2	300	slow	21.55
zz8L-monovacancy-type2	300	fast	21.00
zz8L-monovacancy-type3	1	slow	27.63
zz8L-monovacancy-type3	1	fast	46.41
zz8L-monovacancy-type3	300	slow	21.55
zz8L-monovacancy-type3	300	fast	33.10
zz8L-divacancy-type1	1	slow	34.01
zz8L-divacancy-type1	1	fast	33.10
zz8L-divacancy-type1	300	slow	27.63
zz8L-divacancy-type1	300	fast	33.10
zz8L-divacancy-type2	1	slow	34.01
zz8L-divacancy-type2	1	fast	33.10
zz8L-divacancy-type2	300	slow	27.63
zz8L-divacancy-type2	300	fast	33.10
zz8L-Stone-Wales	1	slow	40.71
zz8L-Stone-Wales	1	fast	46.41
zz8L-Stone-Wales	300	slow	27.63
zz8L-Stone-Wales	300	fast	21.00

figures include strain energy vs. strain graphs drawn according to the raw data listed in Appendix A. Figure 3.2 presents the pristine zigzag GNR which keeps its structure without deformation and fragments suddenly, then stretching is stopped at this point. The same situation holds for the armchair pristine GNR, as well. The graphs shows strain energy with respect to strain. At 1 K, the strain energy vs strain graph under both fast and slow stretching look similar whereas at room temperature they show different behavior. The lines in the graphs are used just to show the connection of data points, hence they do not have any physical meaning. The final length, the number of runs until fragmentation and the failure strain of pristine zigzag GNR are highest among all the defected zigzag GNRs at the same temperature.

Figure 3.3 shows the structure of monovacancy-type1 defected zigzag GNRs at 1 and 300 K under fast and slow stretching processes. By comparing Figure 3.2 and Figure 3.3 it is depicted that the failure strain and final length of the monovacancy-type1 defected GNRs are less than that of pristine GNRs at the same temperature. The pristine model fragments suddenly, however, zigzag GNR with monovacancy-type1 does not preserve its structure until failure, and begins deformation before breakdown. The deformation starts from the edge atoms at 1 K for monovacancy-type1 and bond breaking takes place as shown in Figure 3.3. On the other hand, at 300 K, deformation and bond breaking starts near the defect. The strain vs energy graphs under fast and slow stretching processes show different behavior at 300 K whereas they look similar at 1 K.

It is interesting to note that the deformation at 1 K starts on the edge which is parallel to the side of the triangular type monovacancy. This can be observed clearly by comparing Figure 3.3 and Figure 3.4 on the zigzag GNRs with monovacancy-type2 defect. Actually, there is no significant difference between monovacancy-type1 and monovacancy-type2 in terms of failure strain and strain energy vs strain graph, final length and the number of runs until fragmentation. The final lengths of the zigzag GNRs with monovacancy-type1 and monovacancy-type2 are same at both temperatures and stretching processes. However, the final structure of the ribbons at failure point are different from each other.

Figure 3.5 presents the stretching results of monovacany-type3 defected zigzag GNRs at two

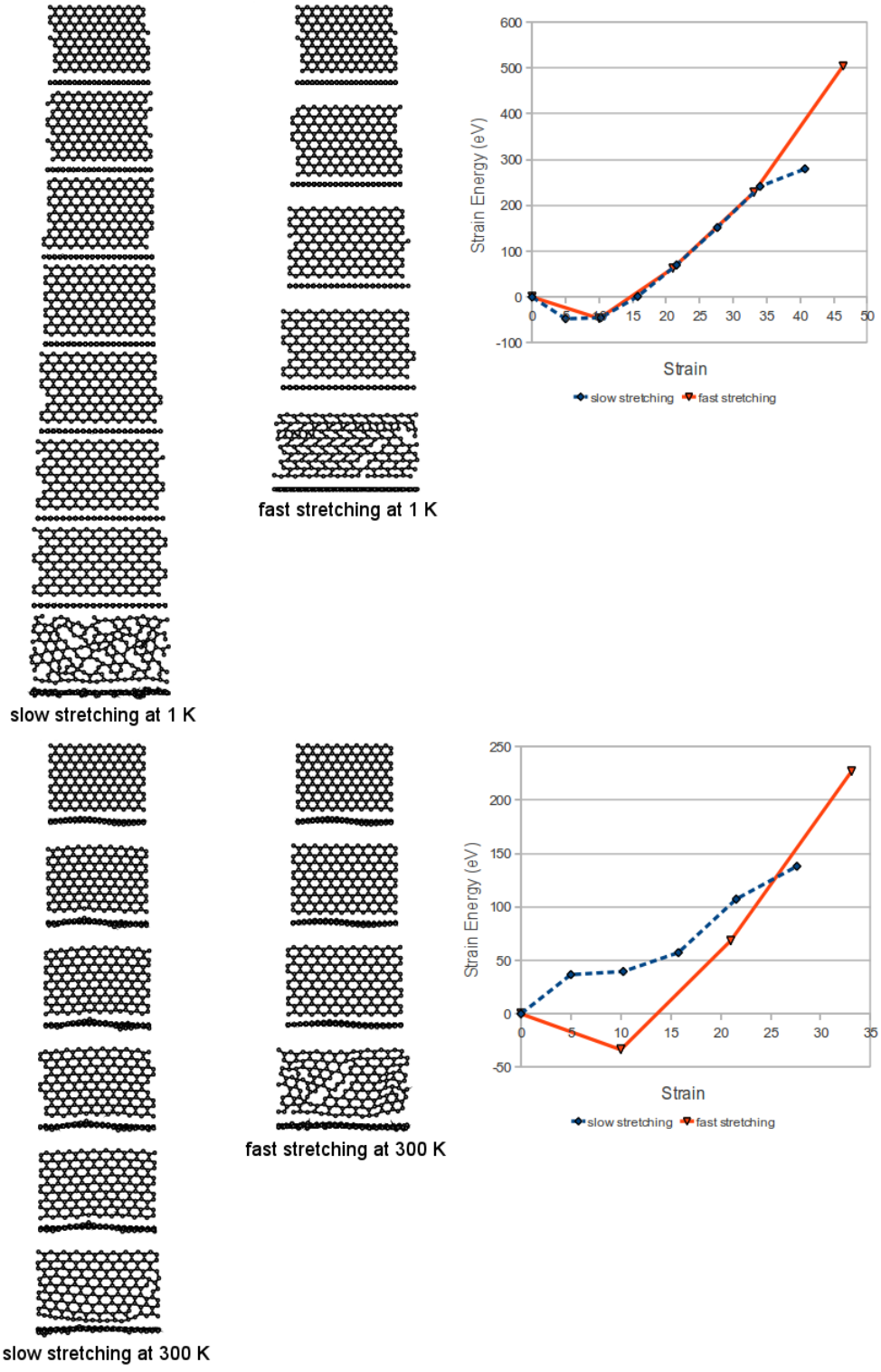

Figure 3.2: Structures of pristine zigzag GNRs under stretch at 1 K and 300 K. Pictures show top and side views. The graphs show strain energy vs. strain for corresponding structures. The lines in the graphs are used just show the connection of data points, they do not have any physical meaning. The same explanation is also valid for the other graphs.

different temperatures. The main difference between monovacancy-type3 and other monovacancy defects is the location of the defect. At monovacancy-type3 the defect is near the edge. However, at the monovacancy-type1 and monovacancy-typ2, defects are in the middle of the GNRs. A comparison of Figures 3.5, 3.3 and 3.4 gives an idea about the effects of the defects' location and shape. At slow stretching, the final length and the failure strain of monovacancy-type3 defected ribbon are less than that of the monovacancy-type1 and monovacancy-type2 at 1K. At room temperature, one of the two differences between the zigzag GNR with monovacancy-type 3 and other monovacancy defected GNRs is the strain energy vs strain graph. The strain energy vs strain graphs of the monovacancy-type1 and monovacancy-type2 defects look similar. However, the strain energy vs strain graph of monovacancy-type3 defect is different than that of others. Secondly, the final length, the failure strain and the number of runs are higher for monovacancy-type3 at room temperature.

Figure 3.6 and Figure 3.7 present the shape of the zigzag GNRs with divacancy-type1 and divacancy-type2, respectively. There is no significant difference between the two figures. The number of stretching runs, failure strain and the final length of the ribbons are the same. The only difference between divacancy-type1 defected GNRs and divacancy-type2 defected GNRs is observed in the strain energy vs strain graph at 300 K.

When divacancy defects and monovacancy defects are compared, it is observed that final length and failure strain of divacancy defected zigzag GNRs are a bit higher than that of monovacancy defected zigzag GNRs at 1 K. On the other hand, they are a bit lower than that of monovacancy defected zigzag GNRs at 300 K. Moreover, side view of the GNR with monovacancy at 300 K is different from the side view of the GNR with divacancy at 300 K. In Figure 3.3 and Figure 3.6, the wavy structure and roughness are localized at the fixed edges of the GNR for monovacancy, whereas the roughness and/or the wavy character are localized close to divacancy position.

Figures 3.8 displays the structures and strain energy vs strain graphs of the Stone-Wales defected zigzag GNRs at 1 and 300 K under fast and slow stretching processes. This model is as strong as pristine model despite of the non-hexoganal bonds, at 1 K. The same conclusion can

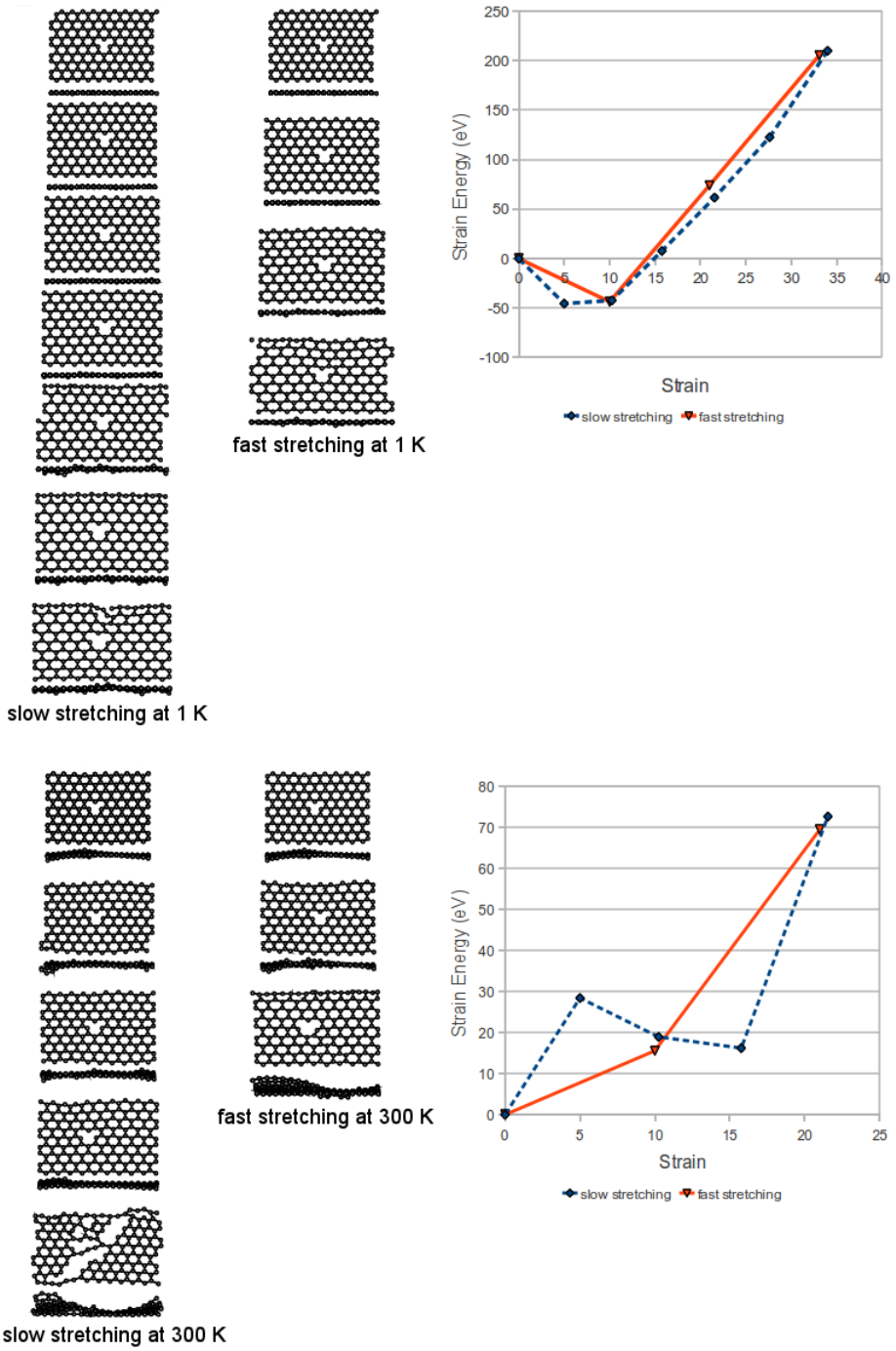

Figure 3.3: Structures of zigzag GNRs with monovacancy-type1 defect under stretch at 1 K and 300 K. Pictures show top and side views. The graphs show strain energy vs. strain for corresponding structures.

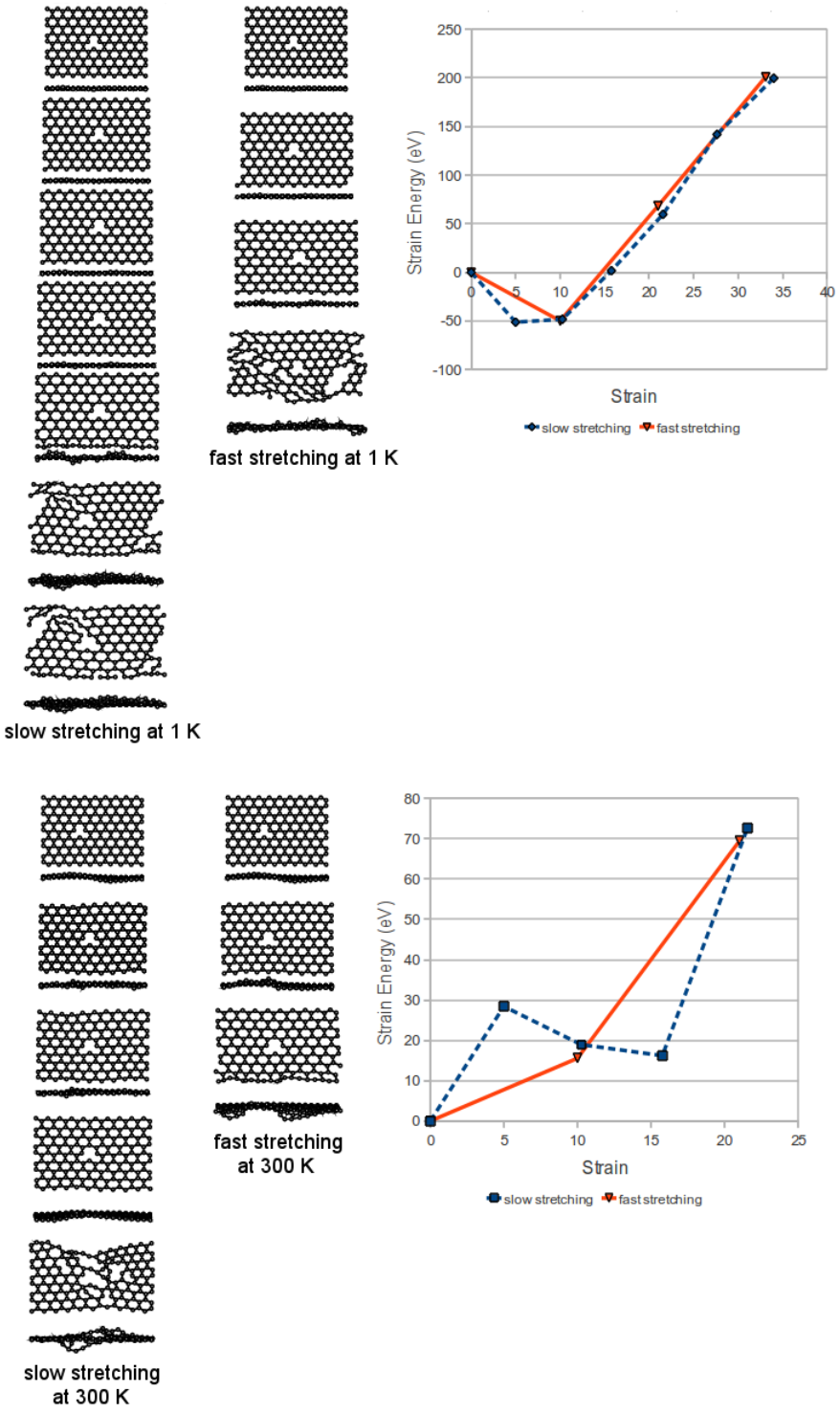

Figure 3.4: Structures of zigzag GNRs with monovacancy-type2 defect under stretch of at 1 K and 300 K. Pictures show top and side views. The graphs show strain energy vs. strain for corresponding structures.

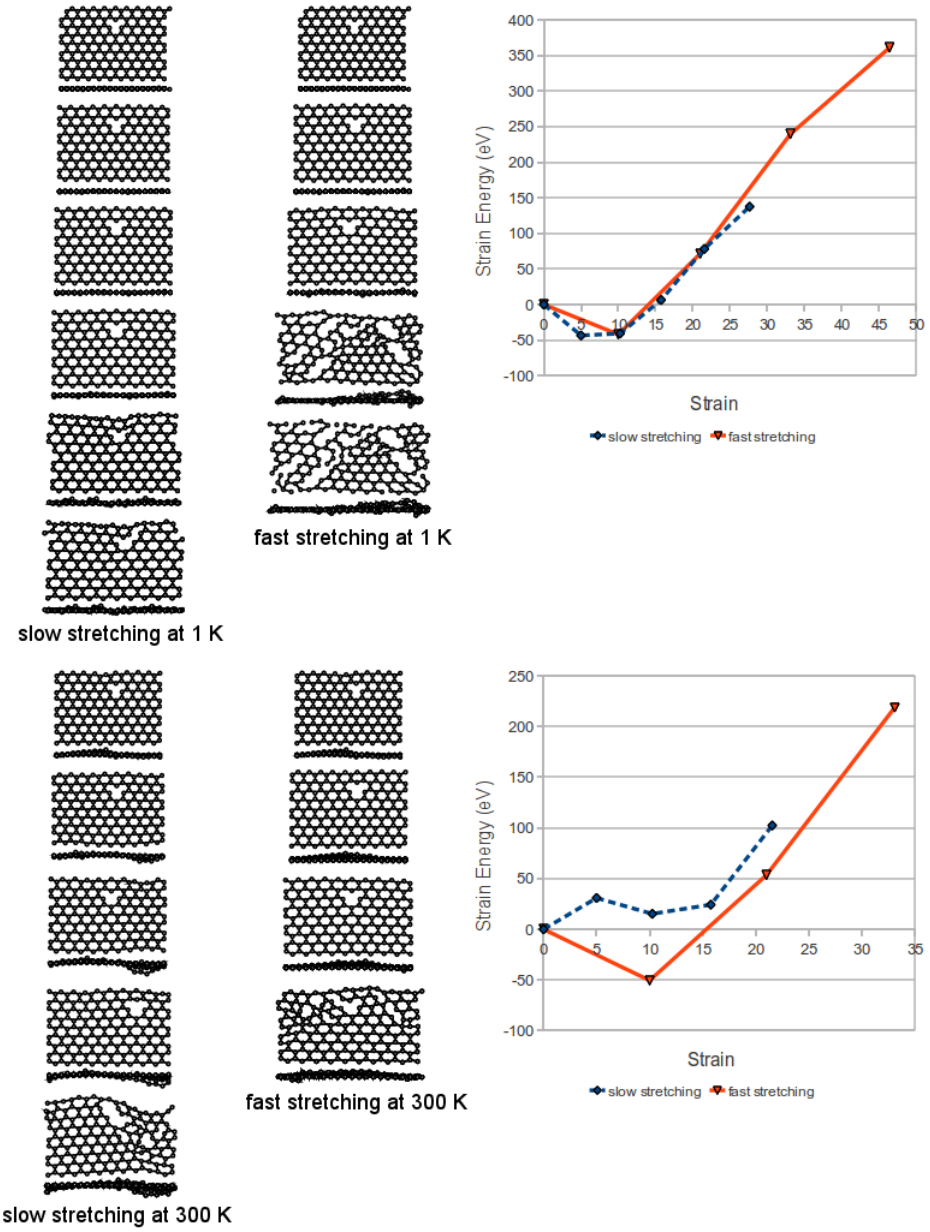

Figure 3.5: Structures of zigzag GNRs with monovacancy-type3 defect under stretch of at 1 K and 300 K. Pictures show top and side views. The graphs show strain energy vs. strain for corresponding structures.

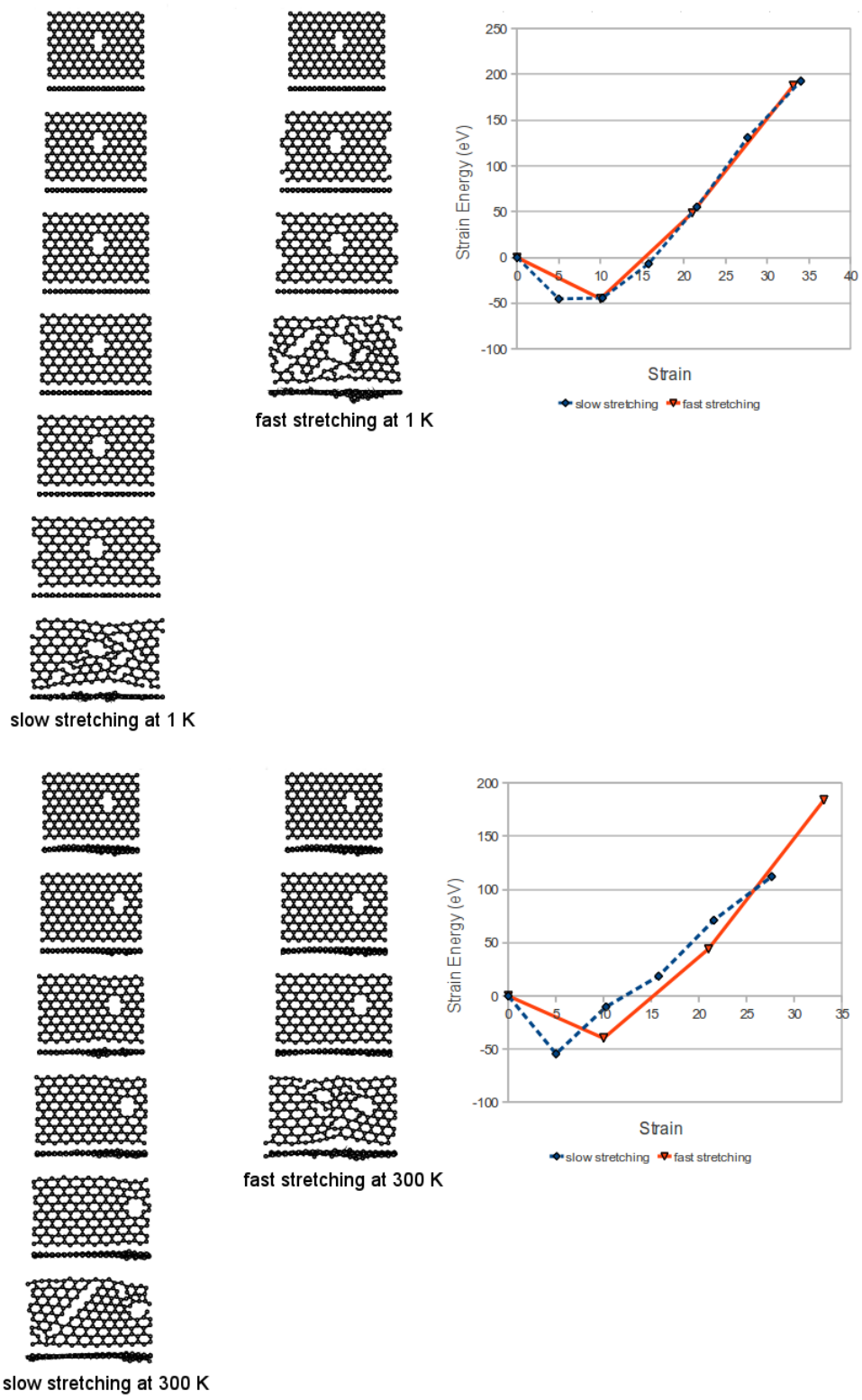

Figure 3.6: Structures of zigzag GNRs with divacancy-type1 defect under stretch at 1 K and 300 K. Pictures show top and side views. The graphs show strain energy vs. strain for corresponding structures.

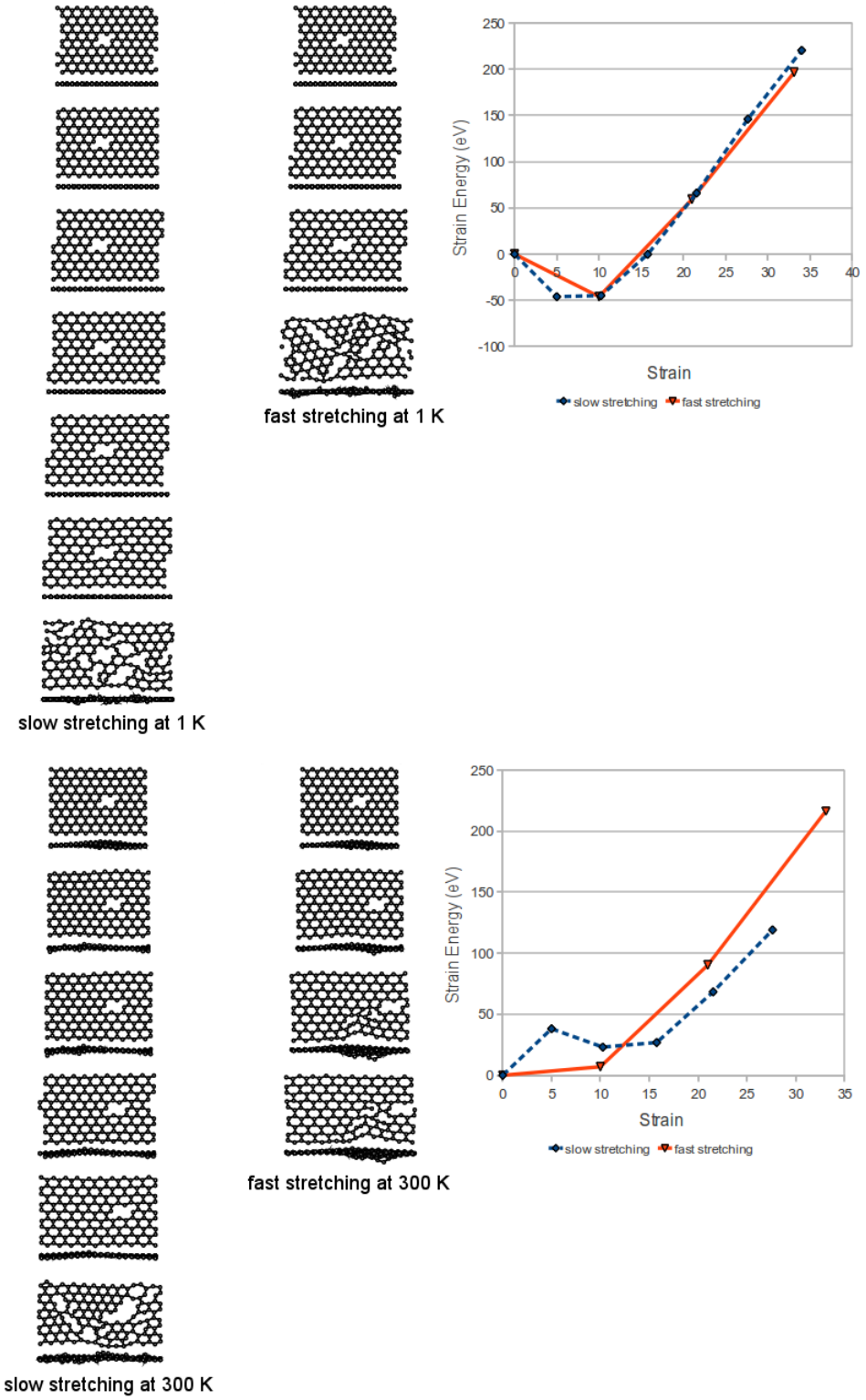

Figure 3.7: Structures of zigzag GNRs with divacancy-type2 defect under stretch at 1 K and 300 K. Pictures show top and side views. The graphs show strain energy vs. strain for corresponding structures.

not be drawn for the model at 300 K. Moreover, the highest strain energy among all zigzag GNRs is obtained in Stone-Wales defected GNR at 1 K. At 1 K, the strain energy vs strain graph under both fast and slow stretching look similar. However, they show different characteristic at 300 K; the strain energy vs strain is larger under slow stretching than that of fast stretching.

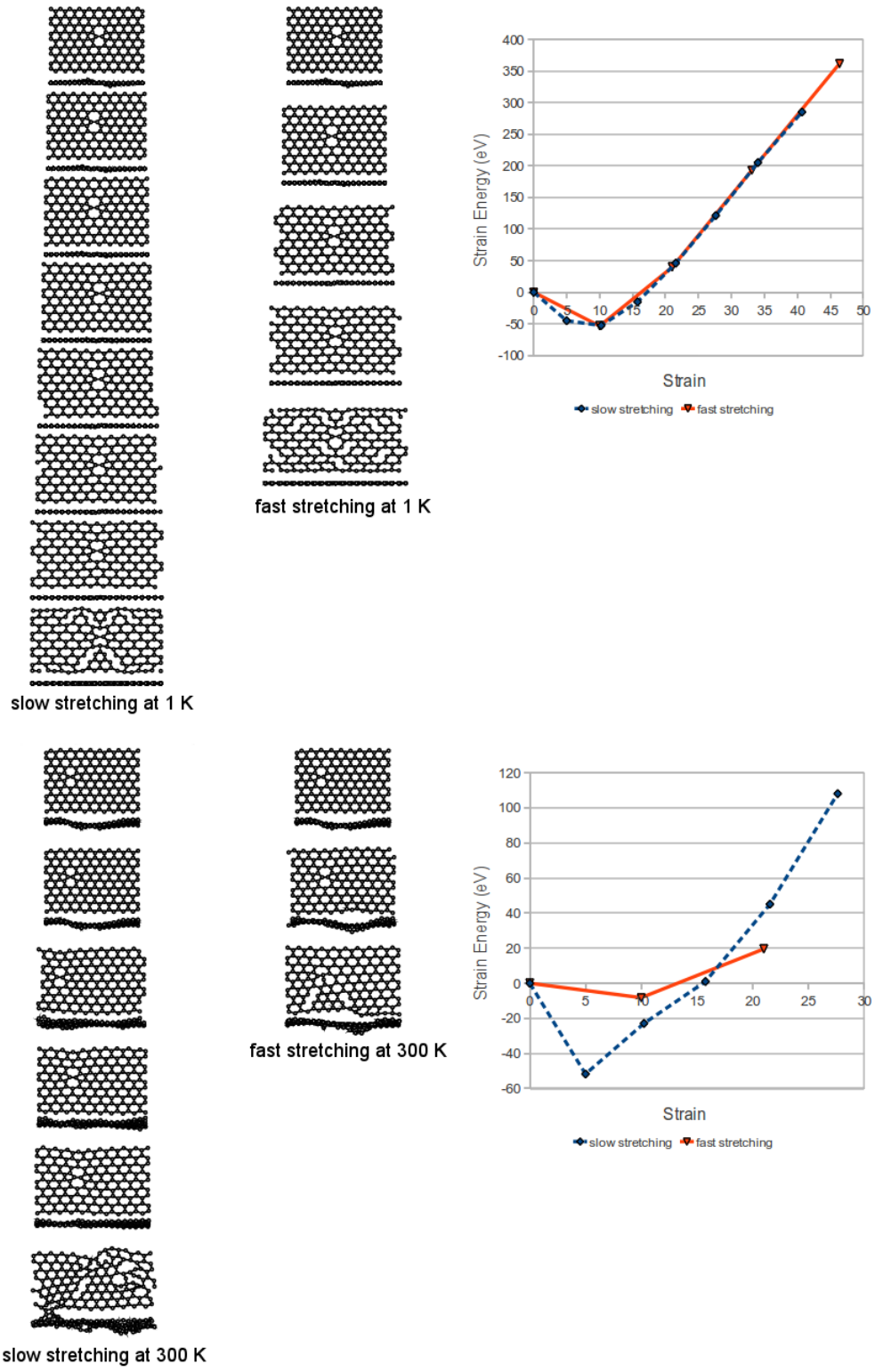

Figure 3.8: Structures of zigzag GNRs with Stone-Wales defect under stretch at 1 K and 300 K. Pictures show top and side views. The graphs show strain energy vs. strain for corresponding structures.

3.2 Armchair GNRs with the Set of Diverse Defects

The set of diverse defects in armchair GNRs is presented in Figure 3.9 with their labels used in this thesis. Defect formation energies, strain values and strain energies are calculated by using total energies and lengths of the structures. The raw data obtained at each stretching step for pristine and defected armchair GNRs is given in Appendix B.

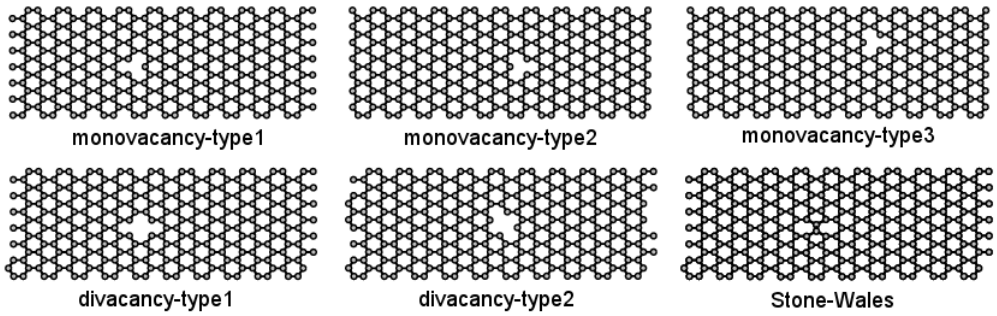

Figure 3.9: A diverse set of defects in armchair GNRs

The calculated formation energies E_{fe} of the defects presented in Figure 3.9 are given in Table 3.3. Being different from zigzag GNRs, defects formation energies of monovacancies/divacancies are close to each other. At 1 K for armchair GNR, formation energy of Stone-Wales defect is calculated as -1.60 eV which is the highest value among all the defect formation energies and the one closest to pristine armchair GNR in terms of total energy. Defected GNR having energy close to the energy of pristine GNR, is more likely to form. Hence, Stone-Wales defect on armchair GNRs is more likely to form at 1 K. At 1 K, Stone-Wales defect on armchair GNR is followed by monovacancy-type3 (-14.50 eV), monovacancy-type1 and monovacancy-type2 (-14.58 eV), divacancy-type1 (-23.52 eV) and divacancy-type2 (-25.43 eV) in terms of tendency to form.

As observed in zigzag GNRs, defect formation energies decrease with increasing temperature for armchair model. Hence, tendency to form defect decreases with increasing temperature for both zigzag and armchair GNRs. Since the amount of decrease are different for each model, E_{fe} of defects might be different despite the equality in the number of missing atoms resulting in defects. At 300 K, the E_{fe} of Stone-Wales defect on armchair GNR decreases drastically

by 1783.2 percent, but it is still the more likely to form among them. At 300 K for armchair GNRs, the defect type can be sorted in descending order in terms of tendency as follows; monovacancy-type2, monovacancy-type1, divacancy-type1, monovacancy-type3, divacancy-type2, Stone-Wales.

Table 3.3: Defect formation energies (E_{fe}, in eV) of armchair 12 layer GNRs

Defect type	**E$_{fe}$ (at 1 K)**	**E$_{fe}$ (at 300 K)**
monovacancy-type1	-14.58	-62.34
monovacancy-type2	-14.58	-87.61
monovacancy-type3	-14.50	-43.24
Stone-Wales	-1.60	-30.13
divacancy-type1	-23.52	-55.44
divacancy-type2	-25.43	-32.50

Strain values calculated at fragmentation point for armchair GNRs are listed in Table 3.4. The maximum strain value is obtained as 46.41 for monovacancy-type2 and divacancy-type2 armchair GNRs at 1 K under fast stretching process. The minimum strain value is obtained as 21.00 for monovacancy-type2, monovacancy-type3, divacancy-type1 and Stone-Wales defected armchair GNRs at 300 K under fast stretching process. As demonstrated in Table 3.4 strain values are affected from temperature. Generally, for armchair GNRs strain values obtained at 300 K are smaller than those at 1K.

The figures 3.10–3.17 show the structure of armchair GNRs under stretching and strain energy vs. strain graphs drawn according to raw data listed in Appendix B. Results of simulations for pristine armchair GNRs at 1 and 300 K are given in Figure 3.10. The number of runs, namely, a complete stretching processes are different under slow and fast stretching processes. For 12 layer armchair GNR model at 1 K, the stretching process continues until 6 runs in slow stretching and 3 runs in fast stretching. It is an expected result since extension is 5 percent for slow stretching whereas it is 10 percent for fast stretching. At 300 K, the topology of GNRs also changes during the stretching process due to temperature. At 1 K, the strain energy vs strain graph under fast and slow stretching processes highly resemble each other. At 300 K, the number of runs, the final length and the failure strain are less than that of pristine armchair ribbon at 1 K, under slow stretching process. However, they are the same under fast

Table 3.4: Calculated failure strain values for pristine and defected armchair GNRs

Graphene model and Defect type	**Temperature (K)**	**Stretching Type**	**Strain**
ac12L-pristine	1	slow	34.01
ac12L-pristine	1	fast	33.10
ac12L-pristine	300	slow	27.63
ac12L-pristine	300	fast	33.10
ac12L-monovacancy-type1	1	slow	34.01
ac12L-monovacancy-type1	1	fast	33.10
ac12L-monovacancy-type1	300	slow	21.55
ac12L-monovacancy-type1	300	fast	33.10
ac12L-monovacancy-type2	1	slow	34.01
ac12L-monovacancy-type2	1	fast	33.10
ac12L-monovacancy-type2	300	slow	21.55
ac12L-monovacancy-type2	300	fast	21.00
ac12L-monovacancy-type3	1	slow	34.01
ac12L-monovacancy-type3	1	fast	46.41
ac12L-monovacancy-type3	300	slow	21.55
ac12L-monovacancy-type3	300	fast	21.00
ac12L-divacancy-type1	1	slow	34.01
ac12L-divacancy-type1	1	fast	46.41
ac12L-divacancy-type1	300	slow	21.55
ac12L-divacancy-type1	300	fast	21.00
ac12L-divacancy-type2	1	slow	26.97
ac12L-divacancy-type2	1	fast	46.41
ac12L-divacancy-type2	300	slow	21.55
ac12L-divacancy-type2	300	fast	33.10
ac12L-Stone-Wales	1	slow	21.55
ac12L-Stone-Wales	1	fast	33.10
ac12L-Stone-Wales	300	slow	27.63
ac12L-Stone-Wales	300	fast	21.00

stretching process at both temperatures. As observed in zigzag models, the topological view of the ribbons at 300 K is a bit wavy that that of the ribbons at 1 K for armchair model.

Figure 3.11 shows the simulations' results of the defected armchair GNR models. These results were obtained at 300 K during slow stretching process. Number of runs are the same for monovacancy and divacancy defected armchair GNR. Moreover, the topology or shape of the GNRs is also similar for monovacancy and divacancy defected armchair GNR. Indeed, these are surpising results since missing of two atoms, instead of one atom, should have a more significant effect on the structure of ribbons. On the other hand, Stone-Wales defected armchair GNR model is stronger than the other defected models. Moreover, non-hexagonal ring changes and becomes a hexagonal ring during the slow stretching process at 300 K. As a result of stretching, a Stone-Wales defected GNR changes to a defect-free GNR namely, Stone-Wales defect disappears during streching process.

Figure 3.12 shows structure of armchair GNRs with monovacancy-type1 defect under stretch at 1 and 300 K. Motion of monovacancy defect at 300 K is more remarkable than that of at 1 K. At 300 K before the stretching process, defects can not be seen clearly in the figure because they move toward the edge. During stretching, movement of defect continues until bond breaking takes place and the structure fragments. The side view of the GNR at 300 K looks more wavy than that of GNR at 1 K due to disarrangement of atoms. However, the side view of the GNR at 1 K is almost smooth. Differently from zigzag model, the number of runs, final length and failure strain of ribbon are the same for pristine and monovacancy-type1 defected armchair ribbon at 1 K during both fast and slow stretching process. However, the strain energy at failure of monovacancy-type1 defected armchair at both stretching are higher than that of pristine armchair. At 300 K, failure strain of monovacancy-type1 is less than that of pristine model under slow stretching process. However, there is no difference between pristine and monovacancy-type1 defected model in terms of runs, failure strain and final length under fast stretching process.

The monovacancy-type2 is presented in Figure 3.13. The side view of the armchair GNR with monovacancy-type2 at 300 K looks more wavy than that of armchair GNR with monovacancy-

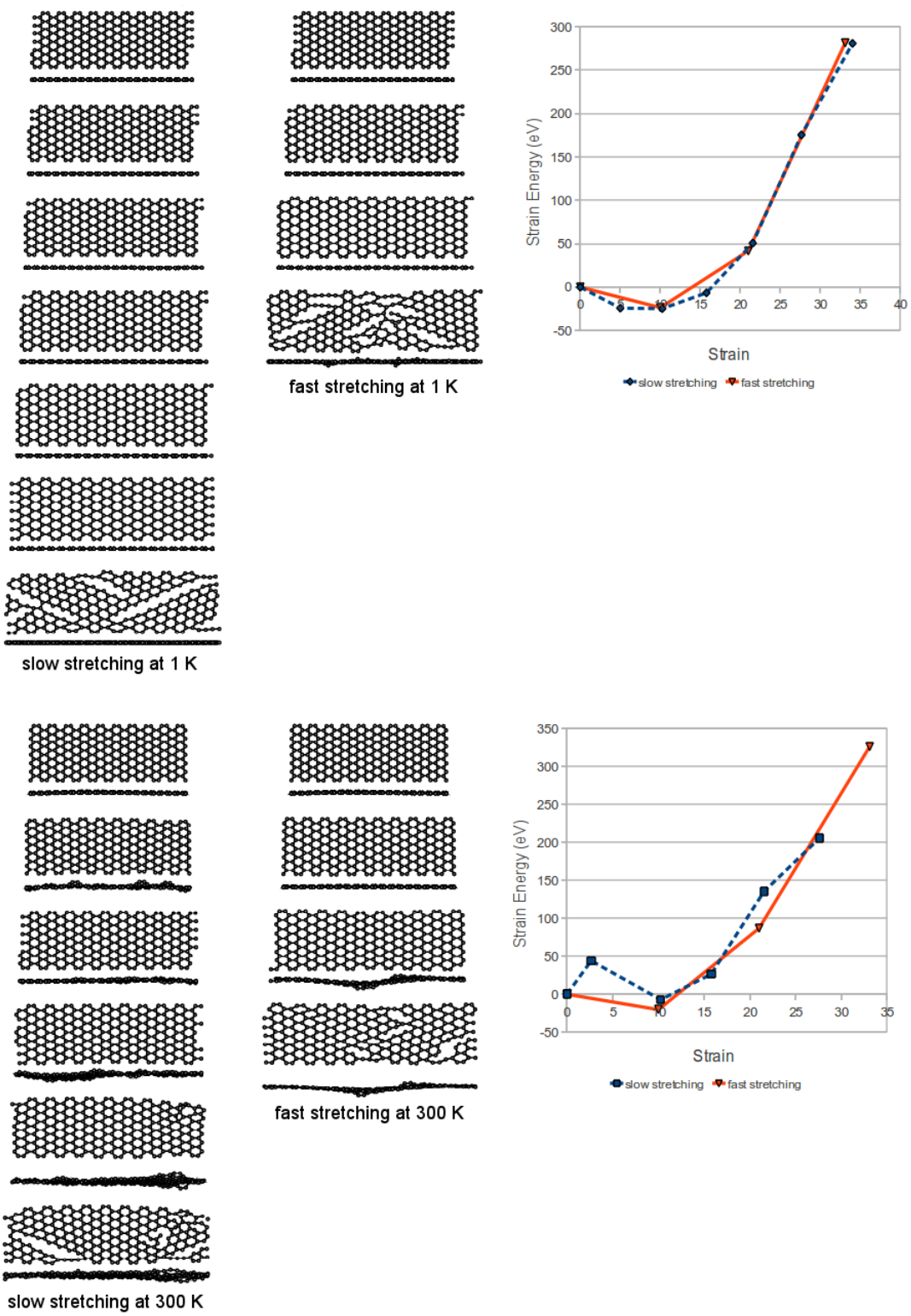

Figure 3.10: Structures of pristine armchair GNRs under stretch at 1 K and 300 K. Pictures show top and side views. The graphs show strain energy vs. strain for corresponding structures.The lines in the graphs are used just show the connection of data points, they do not have any physical meaning. The same explanation is also valid for the other graphs.

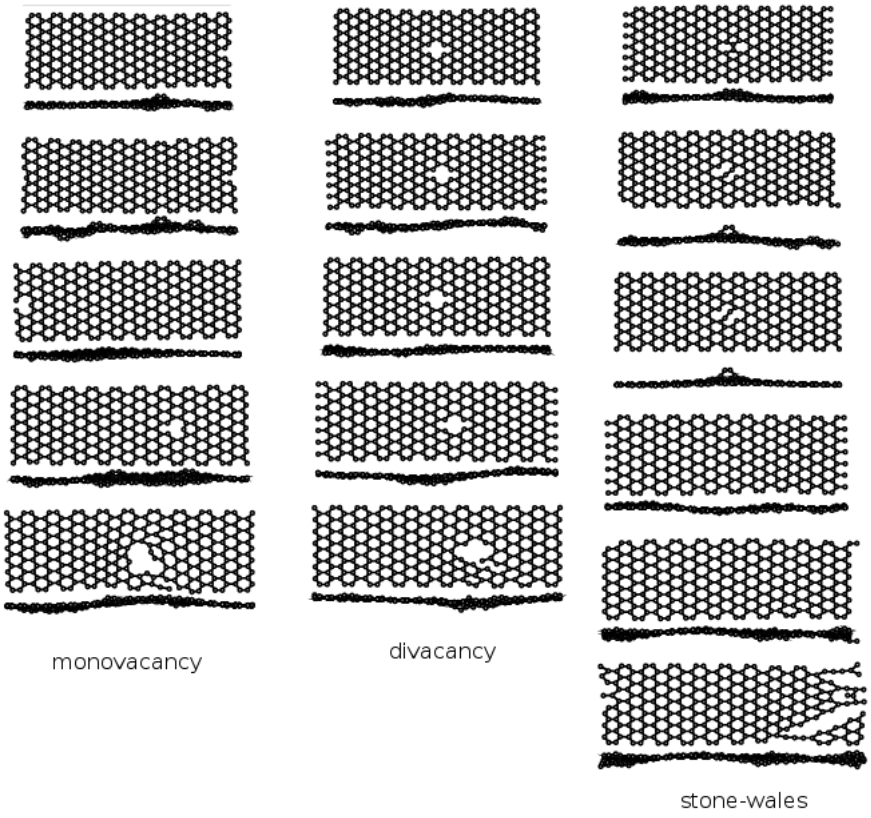

Figure 3.11: Three different structures of defected 12 layer armchair GNRs at 300 K.

type1 and with monovacancy-type3 at 300 K. There is no significant differences between monovacancy-type1 and type2 but the direction of movement of defect. Since the shape of the monovacancy-type1 and type2 are different from each other. The most interesting feature of monovacancy-type2 defect is its strange strain energy-strain graph obtained at room temperature.

The monovacancy-type3 is presented in Figure 3.14. Monovacancy-type3 defected armchair GNR is different than other monocacancies in terms of the location of the defects. This difference does not effect failure strain and final length of the ribbon under slow stretching process. The number of runs and final length of the ribbons of both monovacancy-type1 and monovacancy-type3 are the same at slow stretching process at 1 K and 300 K. Interestingly, the highest failure strain among the armchair ribbons is obtained for this model under fast stretching. Moreover, the number of runs at fast stretching process at 1K of the monovacancy-type3 is higher than that of monovacancy-type1. At 300 K, the strain energy vs. strain graph of monovacancy-type3 defected armchair GNR is as strange as that monovacancy-type2 defected armchair GNR.

Figure 3.15 shows the results of the simulations for armchair GNR with divacancy-type1 defects under stretch. The interesting and more remarkable point in this figure is the growing the size of the defect at 1 K is more rapidly. At the end of the stretching process, the final size of the defect at 1 K is larger than the size of the defect at 300 K.

The divacancy-type2 defect is presented in Figure 3.16. The first difference between divacancy-type1 and divacancy-type2 are the number of the runs and the final length of the ribbons at 300K fast stretching process. However, there is no difference between divacancy-type1 defected GNR and divacancy-type2 defected GNR in terms of failure strain and final length at 1 K. The second difference between them is the shape of the defects at the end of the stretching process. Differently from other defected armchair GNRs at room temperature, the strain energy vs. strain graph of divacancy-type2 defected GNR under fast and slow stretching process possess similar behavior.

The structures and strain energy vs strain graphs of Stone-Wales defected GNR at 1 and 300

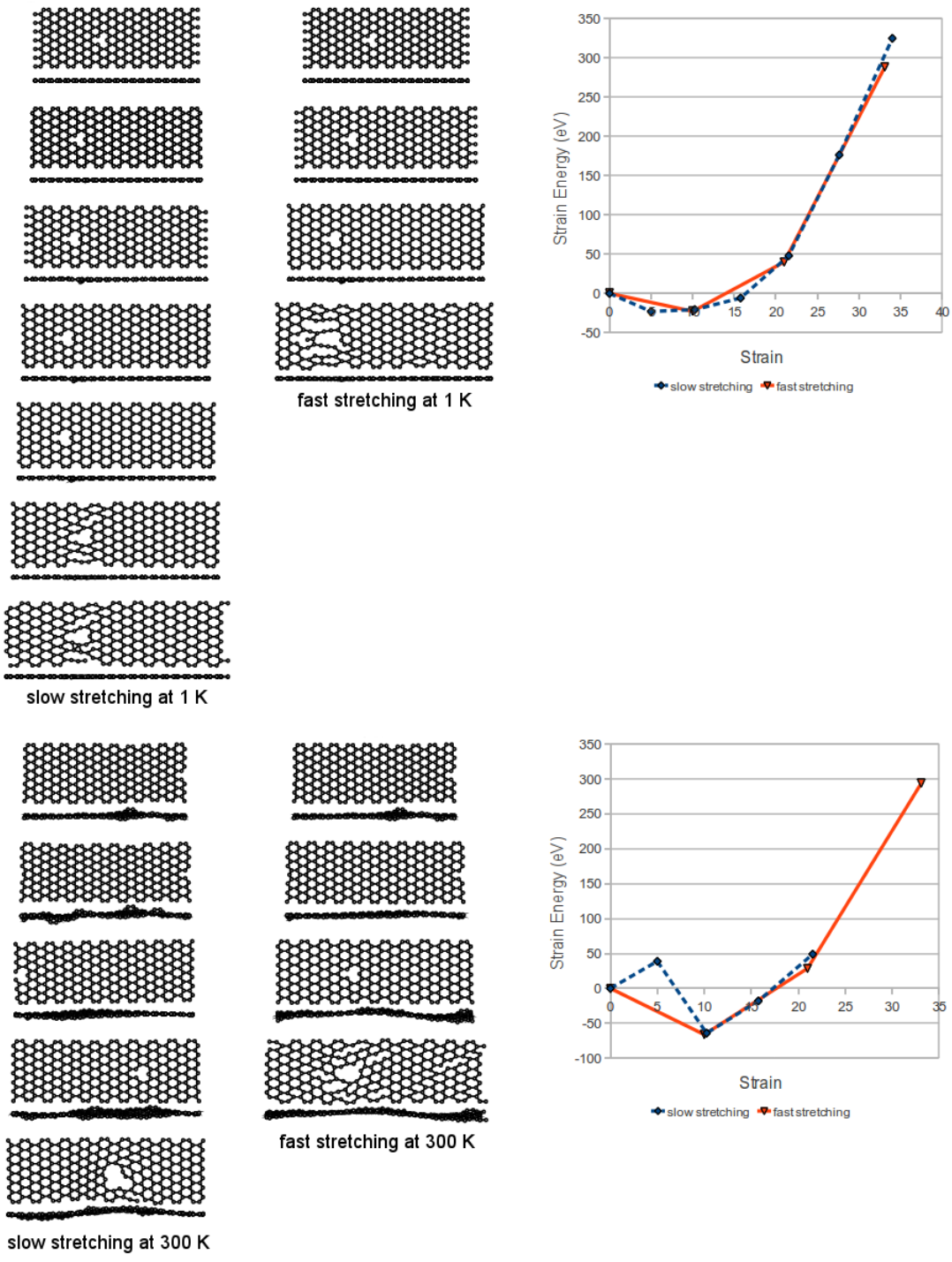

Figure 3.12: Structures of armchair GNRs with monovacancy-type1 defect under stretch at 1 and 300 K. Pictures show top and side views. The graphs show strain energy vs. strain for corresponding structures.

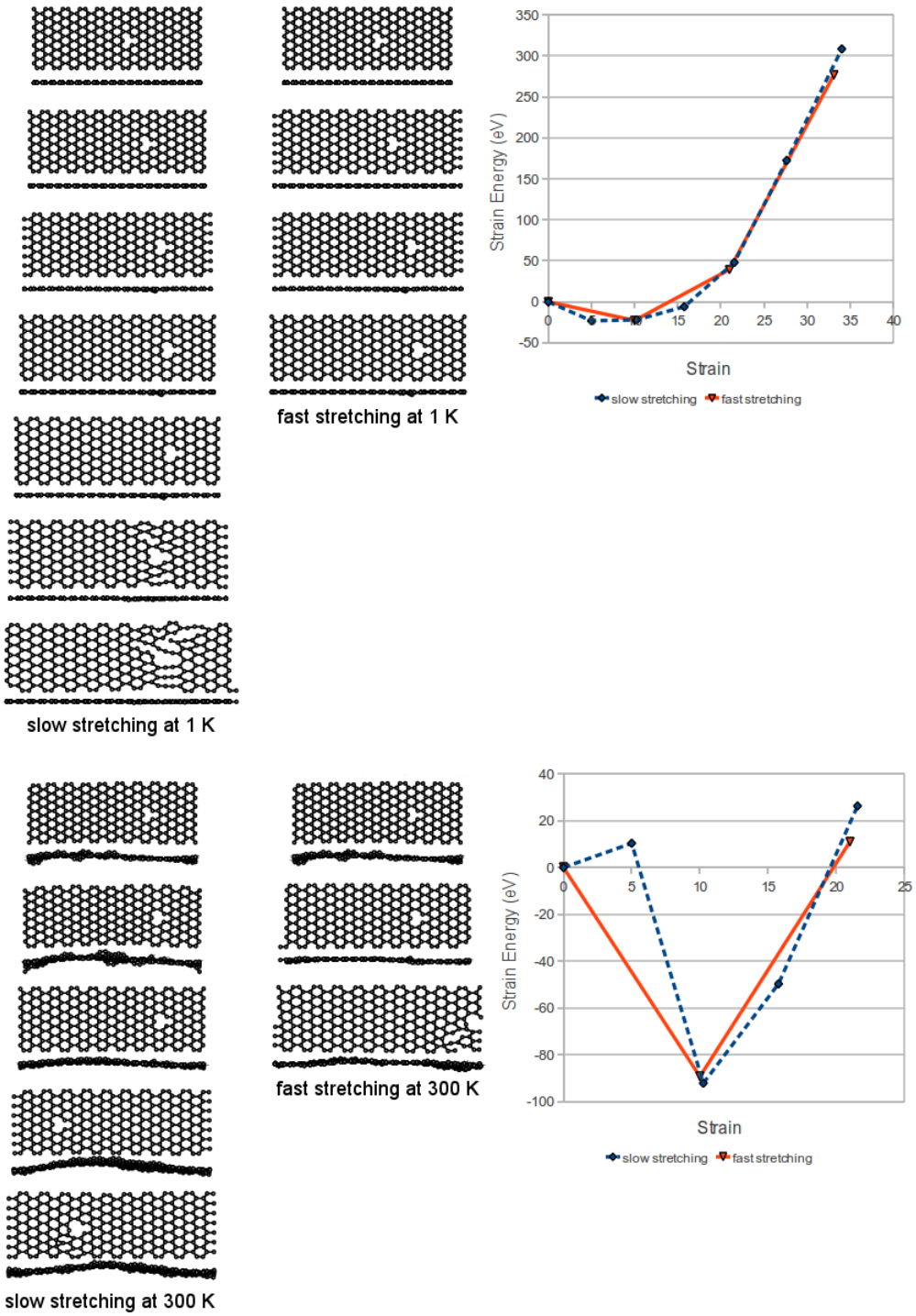

Figure 3.13: Structures of armchair GNRs with monovacancy-type2 defect under stretch at 1 and 300 K. Pictures show top and side views. The graphs show strain energy vs. strain for corresponding structures.

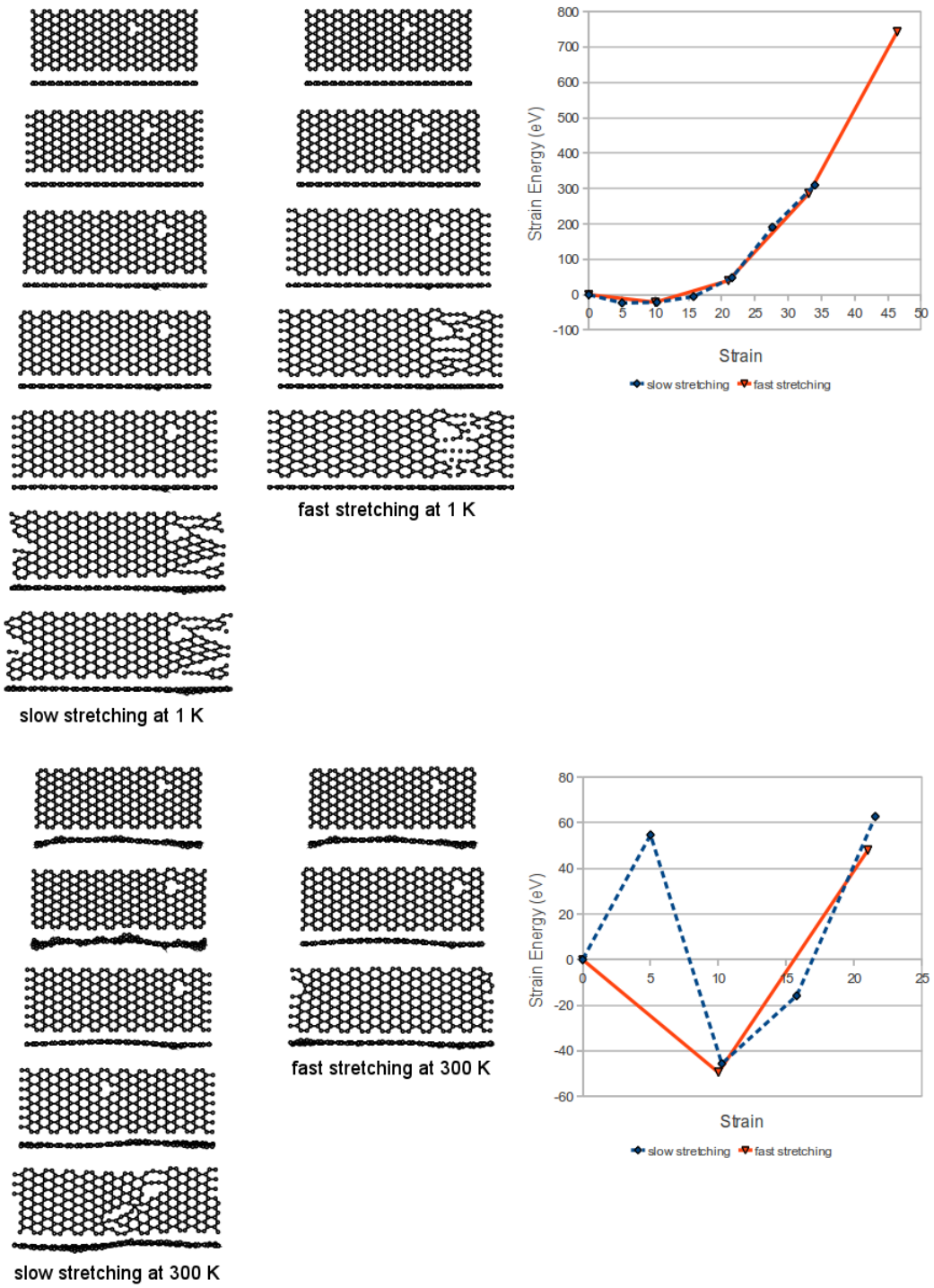

Figure 3.14: Structures of armchair GNRs with monovacancy-type3 defect under stretch at 1 and 300 K. Pictures show top and side views. The graphs show strain energy vs. strain for corresponding structures.

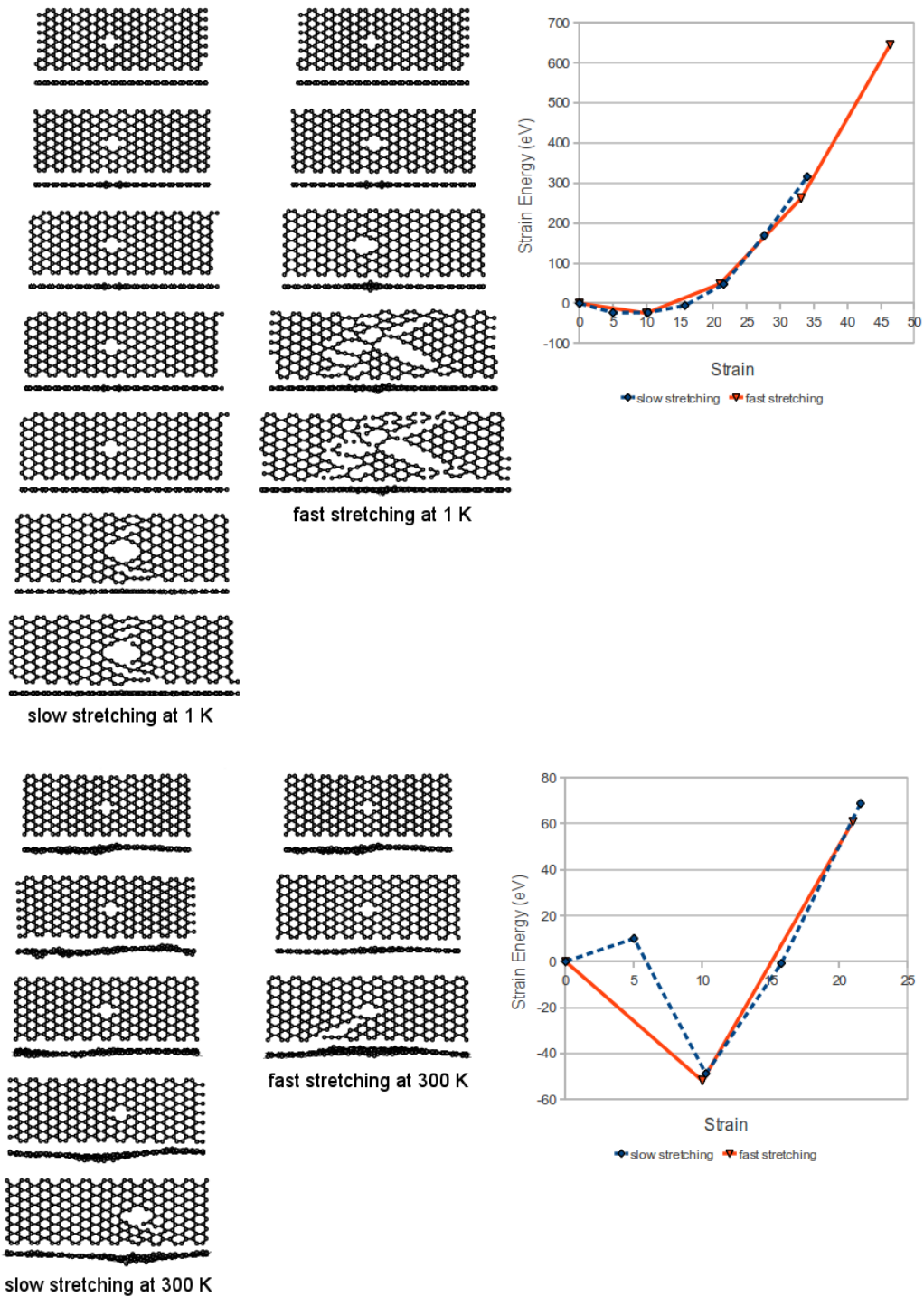

Figure 3.15: Structures of armchair GNRs with divacancy-type1 defect under stretch at 1 and 300 K. Pictures show top and side views. The graphs show strain energy vs. strain for corresponding structures.

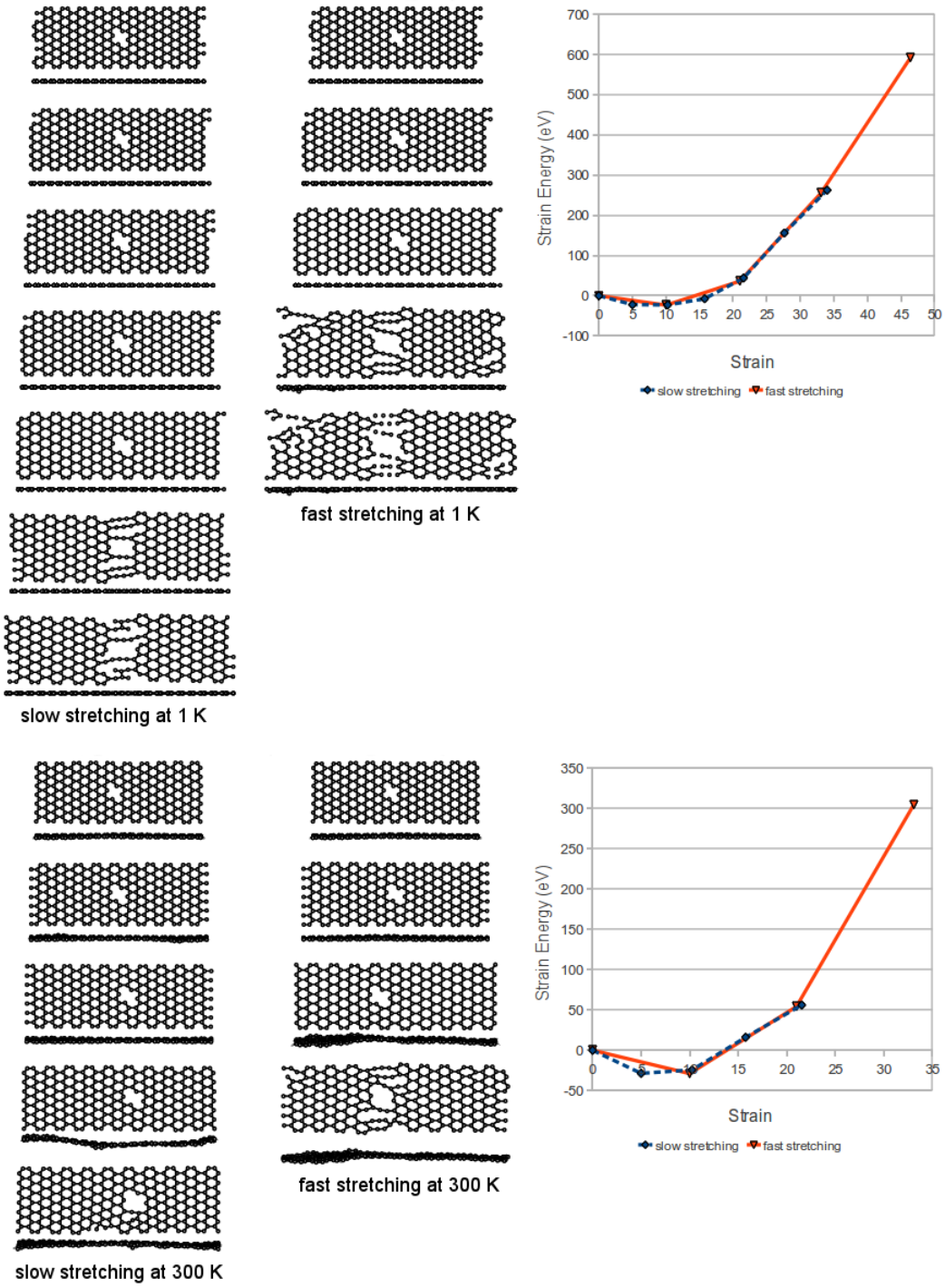

Figure 3.16: Structures of armchair GNRs with divacancy-type2 defect under stretch at 1 and 300 K. Pictures show top and side views. The graphs show strain energy vs. strain for corresponding structures.

K are presented in Figure 3.17. For slow stretching process, the final length, the number of runs and the failure strain value of armchair GNR with STone-Wales defect are smallest among the other armchair GNRs at the same temperature. Stone-Wales defected armchair GNR at room temperature is strongest model among other defected models. Because, non-hexagonal ring changes and becomes a hexagonal ring during slow stretching process at 300 K. The difference between strain energy vs strain graphs at two different temperatures is very interesting, because the characteristics of strain energy vs strain show opposite behaviour at low (1 K) and room temperature (300 K) cases. Strain energy changes rapidly with respect to strain for fast stretching case than that of the slow stretching case at 1 K. On the other hand, the effect is reversed at 300 K, that is, strain energy changes rapidly with respect to strain for slow stretching case than that of the fast stretching case at 300 K.

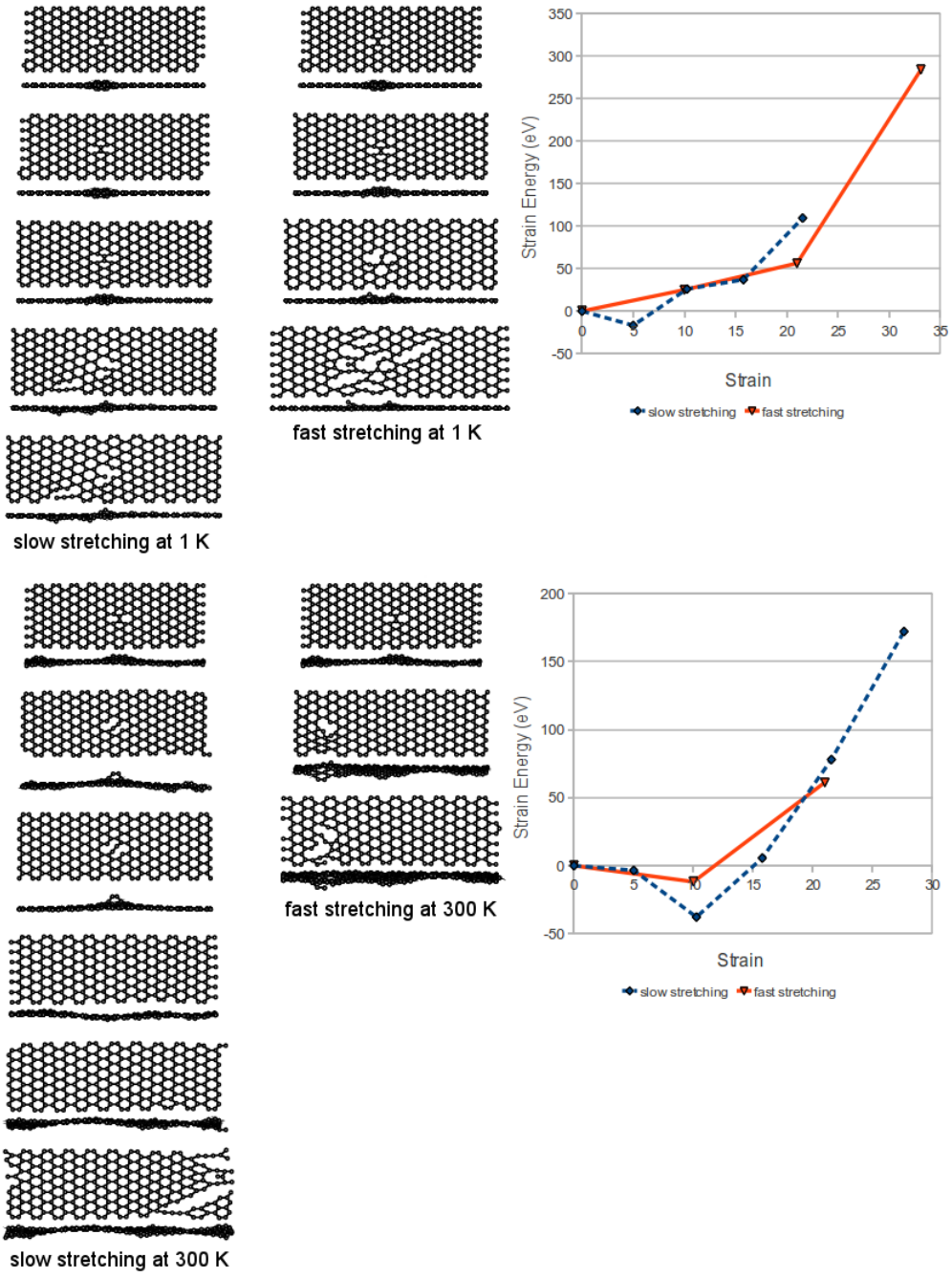

Figure 3.17: Structures of armchair GNRs with Stone-Wales defect under stretch at 1 and 300 K. Pictures show top and side views. The graphs show strain energy vs. strain for corresponding structures.

CHAPTER 4

CONCLUSIONS

In this thesis, we studied pristine and defected GNRs. Strength and stability of armchair and zigzag GNRs at two different temperatures have been investigated by MDS. Results of the simulations were used to calculate strain values, strain energies and defect formation energies. The following conclusions are listed according to the current study. Defect formation energies are affected strongly from temperature and chirality. Defect formation energies are smaller at 300 K than those at 1 K. It can be drawn that formation of defects is easier at low temperatures. At room temperature, mobility of defects can be seen clearly. Moreover, topology and final size of the defects are also affected from temperature. The differences in strength and in stability of zigzag and armchair GNRs can be seen from the differences in defects formation energies and the number of runs in the stretching process. Type of the stretching process (slow or fast) has no significant effect on strain value, whereas it has great effect on strain energy. However, strain value has been affected from both defect and temperature. Strain energy vs. strain graphs are affected by temperature. Mostly, strain energy vs. strain graph under slow and fast stretching show opposite behavior at room temperature. The number of runs, final lengths and failure strain values obtained at 300 K are less than that of those at 1 K. The number of runs taken until fragmentation for zigzag GNRs are slightly more than that of the runs for armchair GNRs. Hence, 8-layer zigzag GNRs are more stable than 12-layer armchair GNRs under stretch.

There are a number of possible further work related to this study. Firstly, the present work can be improved and enhanced by changing certain parameters and modifying the MD program. By increasing length(width) of the ribbons, effect of length(width) on defects formation

energies and strain values can be observed. Young's modulus and Poisson's ratio can be calculated via a few modifications on the MDS code. In the current research, stretching process was carried on only in x direction (uniaxial stretching). Same GNR models can be examined under biaxial tension (stretching both in x and y directions). Strain values and strain energies obtained under biaxial stretching might be different than those under uniaxial stretching. Number of carbon atoms in the zigzag and armchair GNRs are different (180 atoms in zigzag GNR, 280 atoms in armchair GNR). This difference arises from the initial lengths of the ribbons. Due to periodic boundary conditions this difference has no significant effect on the stretching results, however, defect formation energies may be affected from that difference. Defect formation energies can be calculated for zigzag and armchair GNRs by keeping the number of atoms close each other. Hence, the effect of chirality on defect formation energies can be investigated clearly.

REFERENCES

[1] Terrones M., Batello-Mendez A.R., Campos-Delgado J., Lopez-Urias F., Vega-Cantu Y.I., Rodriguez-Macias F.J., et al. Graphene and graphite nanoribbons: morphology, properties, synthesis, defects and applications. *Nano Today* 5: 351-372, 2010.

[2] Banhart F., Kotakoski J., Krasheninnikov A.V. Structural defects in graphene. *ACS Nano* 5: 26-41, 2011.

[3] Soldano C., Mahmood A., Dujardin E. Production, properties and potential of graphene. *Carbon* 48: 2127-2150, 2010.

[4] Miwa R.H., Veiga R.G.A., Srivastava G.P. Structural, electronic, and magnetic properties of pristine and oxygen-adsorbed graphene nanoribbons. *Applied Surface Science* 256: 5776-5782, 2010.

[5] Tao C., Jiao L., Yazyev O.V., Chen Y.C., Feng J., Zhang X., Capaz R.B., Tour J.M., Zettl A., Louie S.G., Dai H., Crommie M.F. Spatially resolving edge states of chiral graphene nanoribbons. *Nature Physics* 7: 616-620, 2011.

[6] Sun B. Formulation of 2D graphene deformation based on chiral-tube base vectors. *Journal of Nanomaterials* 2010: 1-7, 2010.

[7] http://en.wikipedia.org/wiki/Carbon nanotube (last visited February 15 2012).

[8] Nonoselov K.S., Geim A.K., Morozov S.V., Jiang D., Zhang Y., Dubonos S.V., et al. Electric field effect in atomically thin carbon films. *Science* 306: 666-669, 2004.

[9] Brownson D.A.C., Kampouris D.K., Banks C.E. An overview of graphene in energy production and storage applications. *Journal of Power Sources* 196: 4873-4885, 2011.

[10] Chen Z., Lin Y-M., Rooks M.J., Avouris P. Graphene nano-ribbon electronics. *Physica E* 40: 228-232, 2007.

[11] Bai J., Huang Y. Fabrication and electrical properties of graphene nanoribbons. *Materials Science and Engineering R-Reports* 70: 341-353, 2010.

[12] Banerjee S., Bhattacharyya D. Electronic properties of nano-graphene sheets calculated using quantum chemical DFT. *Computational Materials Science* 44: 41-45, 2008.

[13] Peres N.M.R. The electronic properties of graphene and its bilayer. *Vacuum* 83: 1248-1252, 2009.

[14] Geim A.K., Novoselov K.S. Ambipolar electric field effect in single-layer graphene. *Nature Materials* 6: 183-191, 2007.

[15] Novoselov K.S., Geim A.K., Morozov S.V., Jiang D., Katsnelson M.I., Grigorieva I.V., Dubonos S.V., Firsov A.A. Two-dimensional gas of massless Dirac fermions in graphene. *Nature* 438: 197-200, 2005.

[16] Bolotin K.I., Sikes K.J., Jiang Z., Klima M., Fudenberg G., Hone J., Kim P., Stormer H.L. Ultrahigh electron mobility in suspended graphene. *Solid State Communications* 146: 351-355, 2008.

[17] Bu H., Chen Y., Zou M., Yi H., Bi K., Ni Z. Atomistic simulations of mechanical properties of graphene nanoribbons. *Physics Letters A* 373: 3359-3362, 2009.

[18] Lee C., Wei X., Kysar J.W., Hone J. Measurement of the elastic properties and intrinsic strength of monolayer graphene. *Science* 321: 385-388, 2008.

[19] Bunch J.S., Verbridge S.S., Alden J.S., van der Zande A.M., Parpia J.M., Craighead H.G., McEuen P.L. Impermeable atomic membranes from graphene sheets. *Nano Letters*, 8: 2458-2462, 2008.

[20] Bunch J.S., van der Zande A.M., Verbridge S.S., Frank I.W., Tanenbaum D.M., Parpia J.M., Craighead H.G., McEuen P.L. Electromechanical resonators from graphene sheets. *Science* 315: 490-493, 2007.

[21] Q Factor. http://en.wikipedia.org/wiki/factor (Last visited February 9 2012.)

[22] Shao Y., Wang J., Wu H., Liu J., Aksay I.A., Lin Y. Graphene based electrochemical sensors and biosensors: a review. *Electroanalysis* 22: 1027-1036, 2010.

[23] Kuilla T., Bhadra S., Yao D., Kim N.H., Bose S., Lee J.H. Recent advances in graphene based polymer composites. *Progress in Polymer Science* 35: 1350-1375, 2010.

[24] Wu W., Liu Z., Jauregui L.A., Yu Q., Pillai R., Cao H., et al. Wafer scale synthesis of graphene by chemical vapor deposition and its application in hydrogen sensing. *Sensors and Actuators B-Chemical* 150: 296-300, 2010.

[25] Du X., Guo P., Song H., Chen X. Graphene nanosheets as electrode materials for electric double-layer capacitors. *Electrochimica Acta* 55: 4812-4819, 2010.

[26] Wang G., Shen X., Yao J., Park J. Graphene nanosheets for enhanced lithium storage in lithium ion batteris. *Carbon* 47: 2049-2053, 2009.

[27] Bartolucci S.F., Paras J., Rafiee M.A., Rafiee J., Lee S., Kapoor D., et al. Graphene aluminum nanocomposites. *Materials Science and Engineering A-Structural Materials Properties Microstructure and Processing* 528: 7933-7937, 2011.

[28] Rangel E., Ramires-Arellano J.R., Carrillo I., Magana L.F. Hydrogen adsorption around lithium atoms anchored on graphene vacancies. *International Journal of Hydrogen Energy* 36: 13657-13662, 2011.

[29] Cooper D.R., D'Anjau B., Ghattamaneni N., Harack B., Hilke M., Hort A., Majlis N., Massicotte M., Vandsburger L., Whiteway E., Yu, V. Experimental review of graphene. http://arxiv.org/abs/1110.6557 (Last visited on January,2012)

[30] Leon A., Barticevic Z., Pacheco M. Electronic properties of nanoribbon junction. *Microelectronics Journal*, 39: 1239-1241, 2008.

[31] Son Y.-W., Cohen M. L., Louie S. G. Energy gaps in graphene nanoribbons. *Physical Review Letters* 97: 216803-216806, 2006.

[32] Xiong Y.-J., Kong X.-L. Conduction suppression in graphene nanoribbons with a vacancy *Physica B-Condensed Matter*, 405: 1690-1694, 2010.

[33] Georgantzinos S.K., Giannopoulos G.I., Katsareas D.E., Kakavas P.A., Anifantis N.K. Size-dependent non-linear mechanical properties of graphene nanoribbons. *Computational Materials Science* 50: 2057-2062, 2011.

[34] Malcıoğlu O.B. Tailoring one dimensional novel nano structures for specific applications using tools of molecular modeling. PhD Thesis, Middle East Technical University (2008).

[35] Rasuli R., Iraji zad A., Ahadian M.M. Mechanical properties of graphene cantilever from atomic force microscopy and density functional theory. *Nanotechnology* 21: 185503-185509, 2010.

[36] Hod O., Scuseria G.E. Electromechanical properties of suspended graphene nanoribbons. *Nano Letters* 9(7):2619-2622, 2009.

[37] Xu Z. Graphene nano-ribbon under tension. *Journal of Computational and Theoretical Nanoscience*, 6: 625-628, 2009.

[38] Rapaport DC. *The art of molecular dynamics simulation* Cambridge University Press, 1995.

[39] Tersoff J. Emprical interatomic potential for carbon, with applictions to amourpous carbon. *Physical Review Letters* 61: 2879-2882, 1988.

[40] Alder B.J. Wainwright T.E. Phase transition for a hard sphere system. *Journal of Chemical Physics* 27: 1208-1209, 1957.

[41] Thijssen J.M. *Computational Physics* Cambridge University Press, New York, 2007.

[42] Erkoç Ş. Lecture notes on simulations of many particle systems.

[43] Andersen H. C. Molecular dynamics at constant temperature and/or pressure. *Journal of Chemical Physics* 72: 2384-2394, 1980.

[44] Verlet L. Computer ëxperimentsön classical fluids. I. Thermodynamical properties of Lennard-Jones molecules. *Physical Review Letters* 159: 98-103, 1967.

[45] Leach A. R. *Molecular modelling principles and applications* Pearson, Harlow, England, second edition, 2001.

[46] Tersoff J. New empirical approach for the structure and energy of covalent systems. *Physical Review B* 37: 6991-7000, 1988.

[47] Frenkel D. and Smit B. *Understanding Molecular Simulation from algorithms to applications* Academic Press, San Diego, second edition, 2002.

[48] Schofield P. Computer simulation studies of the liquid state. *Computer Physics Communications* 5: 17-23, 1973.

[49] F.J. Vesely, University of Vienna, Periodic boundary conditions (PBC) and nearest image convention (NIC). http://homepage.univie.ac.at/franz.vesely/simsp/dx/node9.html (Last visited on January 2012)

[50] Nose S. A unified formulation of the constant temperature molecular dynamics methods. *Journal of Chemical Physics* 81: 511-519, 1984.

[51] Hoover W.G. Canonical dynamics: Equilibrium phase-space distributions. *Physical Review A* 31: 1695-1697, 1985.

[52] Ma J., Alfè D., Michaelides A., Wang E. Stone-Wales defects in graphene and other planar sp^2-bonded materials. *Physical Review B* 80: 033407(1-4), 2009.

[53] Samsonidze G.G., Yakobson B.I. Energetics of Stone-Wales defects in deformations of monoatomic hexagonal layers. *Computational Materials Science* 23: 62-72, 2002.

[54] Krasheninnikov A.V., Lethinen P.O., Foster A.S., Nieminen R.M. Bending the rules: contrasting vacancy energetics and migration in graphite and carbon nanotubes. *Chemical Physics Letters* 418: 132-136, 2006.

APPENDIX A

STRAIN VALUES AND ENERGIES FOR ZIGZAG GNRs UNDER VARYING STRETCHING TYPES AND TEMPERATURES

Table A.1: Strain values and energies (ΔE) for **pristine** zigzag GNR under slow and fast stretching at **1 K**. At each stretching step, corresponding lengths (L_i) and total energies (E_{total}) are also presented.

Stretching Types	Stretching Steps	L_i (Å)	Strain ($\frac{L_i - L_0}{L_0} \times 100$)	E_{total} (eV)	$\Delta E = (E_i - E_0)$ (eV)
Initial		24.60	0.00	-1173.77	0.00
Slow	1	25.83	5.00	-1221.14	-47.38
	2	27.12	10.25	-1218.94	-45.18
	3	28.48	15.76	-1172.44	1.33
	4	29.90	21.55	-1103.69	70.08
	5	31.40	27.63	-1022.10	151.67
	6	32.97	34.01	-932.29	241.48
	7 (Final)	34.62	40.71	-893.99	276.78
Fast	1	27.06	10.00	-1220.31	-46.54
	2	29.766	21.00	-1110.72	63.05
	3	32.74	33.10	-945.22	228.55
	4 (Final)	36.02	46.41	-669.16	504.61

Table A.2: Strain values and energies (ΔE) for **pristine** zigzag GNR under slow and fast stretching at **300 K**. At each stretching step, corresponding lengths (L_i) and total energies (E_{total}) are also presented.

Stretching Types	Stretching Steps	L_i (Å)	Strain ($\frac{L_i - L_0}{L_0} \times 100$)	E_{total} (eV)	$\Delta E = (E_i - E_0)$ (eV)
Initial		24.60	0.00	-1170.14	0.00
Slow	1	25.83	5.00	-1133.45	36.69
	2	27.12	10.25	-1130.56	39.58
	3	28.48	15.76	-1112.88	57.27
	4	29.90	21.55	-1062.84	107.30
	5 (Final)	31.40	27.63	-1032.12	138.02
Fast	1	27.06	10.00	-1203.71	-33.57
	2	29.77	21.00	-1101.71	68.43
	3 (Final)	32.74	33.10	-943.32	226.82

Table A.3: Strain values and energies (ΔE) for zigzag GNR with **Stone-Wales defect** under slow and fast stretching at **1 K**. At each stretching step, corresponding lengths (L_i) and total energies (E_{total}) are also presented.

Stretching Types	Stretching Steps	L_i (Å)	Strain ($\frac{L_i - L_0}{L_0} \times 100$)	E_{total} (eV)	$\Delta E = (E_i - E_0)$ (eV)
Initial		24.60	0.00	-1146.82	0.00
Slow	1	25.83	5.00	-1191.95	-45.13
	2	27.12	10.25	-1199.41	-52.59
	3	28.48	15.76	-1162.07	-15.25
	4	29.90	21.55	-1100.83	45.99
	5	31.40	27.63	-1025.42	121.40
	6	32.97	34.01	-941.71	205.12
	7 (Final)	34.62	40.71	-861.62	285.20
Fast	1	27.06	10.00	-1200.21	-53.39
	2	29.77	21.00	-1107.27	39.56
	3	32.74	33.10	-953.70	193.12
	4 (Final)	36.02	46.41	-784.92	361.91

Table A.4: Strain values and energies (ΔE) for zigzag GNR with **Stone-Wales defect** under slow and fast stretching at **300 K**. At each stretching step, corresponding lengths (L_i) and total energies (E_{total}) are also presented.

Stretching Types	Stretching Steps	L_i (Å)	Strain ($\frac{L_i - L_0}{L_0} \times 100$)	E_{total} (eV)	$\Delta E = (E_i - E_0)$ (eV)
Initial		24.60	0.00	-1119.56	0.00
Slow	1	25.83	5.00	-1171.29	-51.74
	2	27.12	10.25	-1142.43	-22.87
	3	28.48	15.76	-1118.56	1.00
	4	29.90	21.55	-1074.44	45.12
	5 (Final)	31.40	27.63	-1011.46	108.10
Fast	1	27.06	10.00	-1127.77	-8.22
	2 (Final)	29.77	21.00	-1099.99	19.57

Table A.5: Strain values and energies (ΔE) for zigzag GNR with **monovacancy-type1 defect** under slow and fast stretching at **1 K**. At each stretching step, corresponding lengths (L_i) and total energies (E_{total}) are also presented.

Stretching Types	Stretching Steps	L_i (Å)	Strain ($\frac{L_i - L_0}{L_0} \times 100$)	E_{total} (eV)	$\Delta E = (E_i - E_0)$ (eV)
Initial		24.60	0.00	-1152.30	0.00
Slow	1	25.83	5.00	-1197.78	-45.48
	2	27.12	10.25	-1194.56	-42.26
	3	28.48	15.76	-1144.58	7.72
	4	29.90	21.55	-1090.68	61.62
	5	31.40	27.63	-1029.63	122.67
	6 (Final)	32.97	34.01	-942.21	210.09
Fast	1	27.06	10.00	-1195.87	-43.57
	2	29.77	21.00	-1078.24	74.06
	3 (Final)	32.74	33.10	-946.80	205.50

Table A.6: Strain values and energies (ΔE) for zigzag GNR with **monovacancy-type1 defect** under slow and fast stretching at **300 K**. At each stretching step, corresponding lengths (L_i) and total energies (E_{total}) are also presented.

Stretching Types	Stretching Steps	L_i (Å)	Strain ($\frac{L_i - L_0}{L_0} \times 100$)	E_{total} (eV)	$\Delta E = (E_i - E_0)$ (eV)
Initial		24.60	0.00	-1137.56	0.00
Slow	1	25.83	5.00	-1109.13	28.43
	2	27.12	10.25	-1118.60	18.96
	3	28.48	15.76	-1121.34	16.22
	4 (Final)	29.90	21.55	-1064.89	72.67
Fast	1	27.06	10.00	-1121.99	15.57
	2 (Final)	29.77	21.00	-1068.10	69.46

Table A.7: Strain values and energies (ΔE) for zigzag GNR with **monovacancy-type2 defect** under slow and fast stretching at **1 K**. At each stretching step, corresponding lengths (L_i) and total energies (E_{total}) are also presented.

Stretching Types	Stretching Steps	L_i (Å)	Strain ($\frac{L_i - L_0}{L_0} \times 100$)	E_{total} (eV)	$\Delta E = (E_i - E_0)$ (eV)
Initial		24.60	0.00	-1147.15	0.00
Slow	1	25.83	5.00	-1198.30	-51.15
	2	27.12	10.25	-1195.34	-48.20
	3	28.48	15.76	-1145.33	1.81
	4	29.90	21.55	-1087.50	59.65
	5	31.40	27.63	-1005.22	141.93
	6 (Final)	32.97	34.01	-947.38	199.76
Fast	1	27.06	10.00	-1196.97	-49.82
	2	29.77	21.00	-1078.78	68.37
	3	32.74	33.10	-945.96	201.19

Table A.8: Strain values and energies (ΔE) for zigzag GNR with **monovacancy-type2 defect** under slow and fast stretching at **300 K**. At each stretching step, corresponding lengths (L_i) and total energies (E_{total}) are also presented.

Stretching Types	Stretching Steps	L_i (Å)	Strain ($\frac{L_i - L_0}{L_0} \times 100$)	E_{total} (eV)	$\Delta E = (E_i - E_0)$ (eV)
Initial		24.60	0.00	-1143.46	0.00
Slow	1	25.83	5.00	-1108.49	34.97
	2	27.12	10.25	-1117.74	25.72
	3	28.48	15.76	-1131.24	12.22
	4 (Final)	29.90	21.55	-1043.40	100.06
Fast	1	27.06	10.00	-1147.14	-3.68
	2 (Final)	29.77	21.00	-1067.60	75.86

Table A.9: Strain values and energies (ΔE) for zigzag GNR with **monovacancy-type3 defect** under slow and fast stretching at **1 K**. At each stretching step, corresponding lengths (L_i) and total energies (E_{total}) are also presented.

Stretching Types	Stretching Steps	L_i (Å)	Strain ($\frac{L_i - L_0}{L_0} \times 100$)	E_{total} (eV)	$\Delta E = (E_i - E_0)$ (eV)
Initial		24.60	0.00	-1157.52	0.00
Slow	1	25.83	5.00	-1200.94	-43.42
	2	27.12	10.25	-1198.19	-40.67
	3	28.48	15.76	-1151.00	6.53
	4	29.90	21.55	-1079.36	78.17
	5 (Final)	31.40	27.63	-1019.95	137.57
Fast	1	27.06	10.00	-1199.42	-41.90
	2	29.77	21.00	-1086.03	71.49
	3	32.74	33.10	-918.06	239.47
	4 (Final)	36.02	46.41	-796.57	360.96

Table A.10: Strain values and energies (ΔE) for zigzag GNR with **monovacancy-type3 defect** under slow and fast stretching at **300 K**. At each stretching step, corresponding lengths (L_i) and total energies (E_{total}) are also presented.

Stretching Types	Stretching Steps	L_i (Å)	Strain ($\frac{L_i - L_0}{L_0} \times 100$)	E_{total} (eV)	$\Delta E = (E_i - E_0)$ (eV)
Initial		24.60	0.00	-1144.57	0.00
Slow	1	25.83	5.00	-1113.69	30.89
	2	27.12	10.25	-1129.31	15.26
	3	28.48	15.76	-1120.29	24.28
	4 (Final)	29.90	21.55	-1042.14	102.43
Fast	1	27.06	10.00	-1195.04	-50.47
	2	29.77	21.00	-1091.12	53.45
	3 (Final)	32.74	33.10	-925.67	218.90

Table A.11: Strain values and energies (ΔE) for zigzag GNR with **divacancy-type1 defect** under slow and fast stretching at **1 K**. At each stretching step, corresponding lengths (L_i) and total energies (E_{total}) are also presented.

Stretching Types	Stretching Steps	L_i (Å)	Strain ($\frac{L_i - L_0}{L_0} \times 100$)	E_{total} (eV)	$\Delta E = (E_i - E_0)$ (eV)
Initial		24.60	0.00	-1141.90	0.00
Slow	1	25.83	5.00	-1187.13	-45.23
	2	27.12	10.25	-1186.09	-44.19
	3	28.48	15.76	-1148.79	-6.89
	4	29.90	21.55	-1086.64	55.26
	5	31.40	27.63	-1010.83	131.07
	6 (Final)	32.97	34.01	-949.18	192.72
Fast	1	27.06	10.00	-1186.89	-44.99
	2	29.77	21.00	-1093.16	48.74
	3 (Final)	32.74	33.10	-954.18	187.72

Table A.12: Strain values and energies (ΔE) for zigzag GNR with **divacancy-type1 defect** under slow and fast stretching at **300 K**. At each stretching step, corresponding lengths (L_i) and total energies (E_{total}) are also presented.

Stretching Types	Stretching Steps	L_i (Å)	Strain ($\frac{L_i - L_0}{L_0} \times 100$)	E_{total} (eV)	$\Delta E = (E_i - E_0)$ (eV)
Initial		24.60	0.00	-1126.14	0.00
Slow	1	25.83	5.00	-1180.44	-54.30
	2	27.12	10.25	-1136.36	-10.22
	3	28.48	15.76	-1107.48	18.66
	4	29.90	21.55	-1055.07	71.07
	5 (Final)	31.40	27.63	-1014.04	112.10
Fast	1	27.06	10.00	-1165.83	-39.69
	2	29.77	21.00	-1081.94	44.20
	3 (Final)	32.74	33.10	-942.26	183.88

Table A.13: Strain values and energies (ΔE) for zigzag GNR with **divacancy-type2 defect** under slow and fast stretching at **1 K**. At each stretching step, corresponding lengths (L_i) and total energies (E_{total}) are also presented.

Stretching Types	Stretching Steps	L_i (Å)	Strain ($\frac{L_i - L_0}{L_0} \times 100$)	E_{total} (eV)	$\Delta E = (E_i - E_0)$ (eV)
Initial		24.60	0.00	-1150.36	0.00
Slow	1	25.83	5.00	-1196.33	-45.97
	2	27.12	10.25	-1195.14	-44.78
	3	28.48	15.76	-1150.57	-0.21
	4	29.90	21.55	-1084.29	66.07
	5	31.40	27.63	-1004.16	146.20
	6 (Final)	32.97	34.01	-929.85	220.51
Fast	1	27.06	10.00	-1196.34	-45.98
	2	29.77	21.00	-1091.15	59.21
	3 (Final)	32.74	33.10	-953.80	196.56

Table A.14: Strain values and energies (ΔE) for zigzag GNR with **divacancy-type2 defect** under slow and fast stretching at **300 K**. At each stretching step, corresponding lengths (L_i) and total energies (E_{total}) are also presented.

Stretching Types	Stretching Steps	L_i (Å)	Strain ($\frac{L_i - L_0}{L_0} \times 100$)	E_{total} (eV)	$\Delta E = (E_i - E_0)$ (eV)
Initial		24.60	0.00	-1141.80	0.00
Slow	1	25.83	5.00	-1103.69	38.11
	2	27.12	10.25	-1118.73	23.06
	3	28.48	15.76	-1114.95	26.84
	4	29.90	21.55	-1073.45	68.34
	5 (Final)	31.40	27.63	-1022.69	119.11
Fast	1	27.06	10.00	-1134.83	6.97
	2	29.77	21.00	-1051.51	90.28
	3 (Final)	32.74	33.10	-925.23	216.56

APPENDIX B

STRAIN VALUES AND ENERGIES FOR ARMCHAIR GNRs UNDER VARYING STRETCHING TYPES AND TEMPERATURES

Table B.1: Strain values and energies (ΔE) for **pristine** armchair GNR under slow and fast stretching at **1 K**. At each stretching step, corresponding lengths (L_i) and total energies (E_{total}) are also presented.

Stretching Types	Stretching Steps	L_i (Å)	Strain ($\frac{L_i - L_0}{L_0} \times 100$)	E_{total} (eV)	$\Delta E = (E_i - E_0)$ (eV)
Initial		42.60	0.00	-1830.36	0.00
Slow	1	44.73	5.00	-1854.53	-24.17
	2	46.97	10.25	-1855.06	-24.70
	3	49.32	15.76	-1836.87	-6.52
	4	51.78	21.55	-1779.64	50.72
	5	54.37	27.63	-1654.91	175.45
	6 (Final)	57.09	34.01	-1549.52	280.84
Fast	1	46.86	10.00	-1853.97	-23.61
	2	51.55	21.00	-1788.55	41.81
	3 (Final)	56.70	33.10	-1548.79	281.57

Table B.2: Strain values and energies (ΔE) for **pristine** armchair GNR under slow and fast stretching at **300 K**. At each stretching step, corresponding lengths (L_i) and total energies (E_{total}) are also presented.

Stretching Types	Stretching Steps	L_i (Å)	Strain ($\frac{L_i - L_0}{L_0} \times 100$)	E_{total} (eV)	$\Delta E = (E_i - E_0)$ (eV)
Initial		42.60	0.00	-1839.86	0.00
Slow	1	44.73	5.00	-1795.72	44.13
	2	46.97	10.25	-1847.03	-7.17
	3	49.32	15.76	-1813.44	26.42
	4	51.78	21.55	-1704.44	135.42
	5 (Final)	54.37	27.63	-1634.07	205.79
Fast	1	46.86	10.00	-1860.12	-20.26
	2	51.55	21.00	-1752.98	86.88
	3 (Final)	56.70	33.10	-1513.69	326.17

Table B.3: Strain values and energies (ΔE) for armchair GNR with **Stone-Wales defect** under slow and fast stretching at **1 K**. At each stretching step, corresponding lengths (L_i) and total energies (E_{total}) are also presented.

Stretching Types	Stretching Steps	L_i (Å)	Strain ($\frac{L_i - L_0}{L_0} \times 100$)	E_{total} (eV)	$\Delta E = (E_i - E_0)$ (eV)
Initial		42.60	0.00	-1828.76	0.00
Slow	1	44.73	5.00	-1845.61	-16.84
	2	46.97	10.25	-1802.82	25.94
	3	49.32	15.76	-1791.72	37.04
	4 (Final)	51.78	21.55	-1719.27	109.49
Fast	1	46.86	10.00	-1803.72	25.04
	2	51.55	21.00	-1772.45	56.31
	3 (Final)	56.70	33.10	-1544.88	283.89

Table B.4: Strain values and energies (ΔE) for armchair GNR with **Stone-Wales defect** under slow and fast stretching at **300 K**. At each stretching step, corresponding lengths (L_i) and total energies (E_{total}) are also presented.

Stretching Types	Stretching Steps	L_i (Å)	Strain ($\frac{L_i - L_0}{L_0} \times 100$)	E_{total} (eV)	$\Delta E = (E_i - E_0)$ (eV)
Initial		42.60	0.00	-1809.73	0.00
Slow	1	44.73	5.00	-1813.20	-3.47
	2	46.97	10.25	-1847.49	-37.76
	3	49.32	15.76	-1804.16	5.57
	4	51.78	21.55	-1731.73	78.00
	5 (Final)	54.37	27.63	-1637.67	172.06
Fast	1	46.86	10.00	-1821.59	-11.86
	2 (Final)	51.55	21.00	-1748.51	61.22

Table B.5: Strain values and energies (ΔE) for armchair GNR with **monovacancy-type1 defect** under slow and fast stretching at **1 K**. At each stretching step, corresponding lengths (L_i) and total energies (E_{total}) are also presented.

Stretching Types	Stretching Steps	L_i (Å)	Strain ($\frac{L_i - L_0}{L_0} \times 100$)	E_{total} (eV)	$\Delta E = (E_i - E_0)$ (eV)
Initial		42.60	0.00	-1815.78	0.00
Slow	1	44.73	5.00	-1838.82	-23.05
	2	46.97	10.25	-1836.47	-20.70
	3	49.32	15.76	-1821.72	-5.95
	4	51.78	21.55	-1767.89	47.88
	5	54.37	27.63	-1639.44	176.34
	6 (Final)	57.09	34.01	-1490.96	324.81
Fast	1	46.86	10.00	-1838.61	-22.84
	2	51.55	21.00	-1775.89	39.88
	3 (Final)	56.70	33.10	-1527.53	288.25

Table B.6: Strain values and energies (ΔE) for armchair GNR with **monovacancy-type1 defect** under slow and fast stretching at **300 K**. At each stretching step, corresponding lengths (L_i) and total energies (E_{total}) are also presented.

Stretching Types	Stretching Steps	L_i (Å)	Strain ($\frac{L_i - L_0}{L_0} \times 100$)	E_{total} (eV)	$\Delta E = (E_i - E_0)$ (eV)
Initial		42.60	0.00	-1777.52	0.00
Slow	1	44.73	5.00	-1738.67	38.85
	2	46.97	10.25	-1841.62	-64.10
	3	49.32	15.76	-1795.55	-18.03
	4 (Final)	51.78	21.55	-1728.50	49.02
Fast	1	46.86	10.00	-1843.66	-66.14
	2	51.55	21.00	-1748.81	28.71
	3 (Final)	56.70	33.10	-1483.91	293.61

Table B.7: Strain values and energies (ΔE) for armchair GNR with **monovacancy-type2 defect** under slow and fast stretching at **1 K**. At each stretching step, corresponding lengths (L_i) and total energies (E_{total}) are also presented.

Stretching Types	Stretching Steps	L_i (Å)	Strain ($\frac{L_i - L_0}{L_0} \times 100$)	E_{total} (eV)	$\Delta E = (E_i - E_0)$ (eV)
Initial		42.60	0.00	-1815.78	0.00
Slow	1	44.73	5.00	-1838.91	-23.13
	2	46.97	10.25	-1837.72	-21.95
	3	49.32	15.76	-1821.76	-5.98
	4	51.78	21.55	-1767.85	47.93
	5	54.37	27.63	-1643.25	172.52
	6 (Final)	57.09	34.01	-1507.24	308.54
Fast	1	46.86	10.00	-1838.58	-22.80
	2	51.55	21.00	-1776.33	39.45
	3 (Final)	56.70	33.10	-1538.76	277.02

Table B.8: Strain values and energies (ΔE) for armchair GNR with **monovacancy-type2 defect** under slow and fast stretching at **300 K**. At each stretching step, corresponding lengths (L_i) and total energies (E_{total}) are also presented.

Stretching Types	Stretching Steps	L_i (Å)	Strain ($\frac{L_i - L_0}{L_0} \times 100$)	E_{total} (eV)	$\Delta E = (E_i - E_0)$ (eV)
Initial		42.60	0.00	-1752.25	0.00
Slow	1	44.73	5.00	-1741.89	10.36
	2	46.97	10.25	-1844.34	-92.09
	3	49.32	15.76	-1801.93	-49.68
	4 (Final)	51.78	21.55	-1725.98	26.28
Fast	1	46.86	10.00	-1841.52	-89.27
2 (Final)	51.55	21.00	-1741.22	11.03	

Table B.9: Strain values and energies (ΔE) for armchair GNR with **monovacancy-type3 defect** under slow and fast stretching at **1 K**. At each stretching step, corresponding lengths (L_i) and total energies (E_{total}) are also presented.

Stretching Types	Stretching Steps	L_i (Å)	Strain ($\frac{L_i - L_0}{L_0} \times 100$)	E_{total} (eV)	$\Delta E = (E_i - E_0)$ (eV)
Initial		42.60	0.00	-1815.86	0.00
Fast	1	44.73	5.00	-1839.36	-23.51
	2	46.97	10.25	-1837.50	-21.64
	3	49.32	15.76	-1821.18	-5.32
	4	51.78	21.55	-1767.67	48.19
	5	54.37	27.63	-1624.97	190.89
	6 (Final)	57.09	34.01	-1506.26	309.60
Fast	1	46.86	10.00	-1837.33	-21.48
	2	51.55	21.00	-1775.99	39.87
	3	56.70	33.10	-1530.44	285.42
	4	62.37	46.41	-1072.61	743.25

Table B.10: Strain values and energies (ΔE) for armchair GNR with **monovacancy-type3 defect** under slow and fast stretching at **300 K**. At each stretching step, corresponding lengths (L_i) and total energies (E_{total}) are also presented.

Stretching Types	Stretching Steps	L_i (Å)	Strain ($\frac{L_i - L_0}{L_0} \times 100$)	E_{total} (eV)	$\Delta E = (E_i - E_0)$ (eV)
Initial		42.60	0.00	-1796.62	0.00
Slow	1	44.73	5.00	-1741.91	54.71
	2	46.97	10.25	-1842.25	-45.63
	3	49.32	15.76	-1812.43	-15.82
	4 (Final)	51.78	21.55	-1733.86	62.76
Fast	1	46.86	10.00	-1846.09	-49.47
	2 (Final)	51.55	21.00	-1748.63	47.98

Table B.11: Strain values and energies (ΔE) for armchair GNR with **divacancy-type1 defect** under slow and fast stretching at **1 K**. At each stretching step, corresponding lengths (L_i) and total energies (E_{total}) are also presented.

Stretching Types	Stretching Steps	L_i (Å)	Strain ($\frac{L_i - L_0}{L_0} \times 100$)	E_{total} (eV)	$\Delta E = (E_i - E_0)$ (eV)
Initial		42.60	0.00	-1806.84	0.00
Slow	1	44.73	5.00	-1830.15	-23.31
	2	46.97	10.25	-1830.04	-23.20
	3	49.32	15.76	-1812.29	-5.45
	4	51.78	21.55	-1759.09	47.75
	5	54.37	27.63	-1637.61	169.23
	6 (Final)	57.09	34.01	-1491.11	315.73
Fast	1	46.86	10.00	-1831.51	-24.67
	2	51.55	21.00	-1758.05	48.79
	3	56.70	33.10	-1545.20	216.64
	4 (Final)	62.37	46.41	-1161.73	645.11

Table B.12: Strain values and energies (ΔE) for armchair GNR with **divacancy-type1 defect** under slow and fast stretching at **300 K**. At each stretching step, corresponding lengths (L_i) and total energies (E_{total}) are also presented.

Stretching Types	Stretching Steps	L_i (Å)	Strain ($\frac{L_i - L_0}{L_0} \times 100$)	E_{total} (eV)	$\Delta E = (E_i - E_0)$ (eV)
Initial		42.60	0.00	-1784.42	0.00
Slow	1	44.73	5.00	-1774.39	10.03
	2	46.97	10.25	-1833.21	-48.79
	3	49.32	15.76	-1785.21	-0.79
	4 (Final)	51.78	21.55	-1715.59	68.83
Fast	1	46.86	10.00	-1836.35	-51.93
	2 (Final)	51.55	21.00	-1723.42	61.00

Table B.13: Strain values and energies (ΔE) for armchair GNR with **divacancy-type2 defect** under slow and fast stretching at **1 K**. At each stretching step, corresponding lengths (L_i) and total energies (E_{total}) are also presented.

Stretching Types	Stretching Steps	L_i (Å)	Strain ($\frac{L_i - L_0}{L_0} \times 100$)	E_{total} (eV)	$\Delta E = (E_i - E_0)$ (eV)
Initial		42.60	0.00	-1804.93	0.00
Slow	1	44.73	5.00	-1827.22	-22.29
	2	46.97	10.25	-1827.85	-22.92
	3	49.32	15.76	-1812.49	-7.56
	4	51.78	21.55	-1761.08	43.85
	5	54.37	27.63	-1649.01	155.92
	6 (Final)	57.09	34.01	-1542.39	262.54
Fast	1	46.86	10.00	-1828.49	-23.56
	2	51.55	21.00	-1768.84	36.09
	3	56.70	33.10	-1549.41	255.52
	4 (Final)	62.37	46.41	-1213.19	591.74

Table B.14: Strain values and energies (ΔE) for armchair GNR with **divacancy-type2 defect** under slow and fast stretching at **300 K**. At each stretching step, corresponding lengths (L_i) and total energies (E_{total}) are also presented.

Stretching Types	Stretching Steps	L_i (Å)	Strain ($\frac{L_i - L_0}{L_0} \times 100$)	E_{total} (eV)	$\Delta E = (E_i - E_0)$ (eV)
Initial		42.60	0.00	-1807.36	0.00
Slow	1	44.73	5.00	-1835.99	-28.64
	2	46.97	10.25	-1831.76	-24.41
	3	49.32	15.76	-1791.32	16.04
	4 (Final)	51.78	21.55	-1751.31	56.04
Fast	1	46.86	10.00	-1836.29	-28.94
	2	51.55	21.00	-1753.20	54.16
	3 (Final)	56.70	33.10	-1502.61	304.74

APPENDIX C

FLOW CHART OF THE MDS PROGRAM

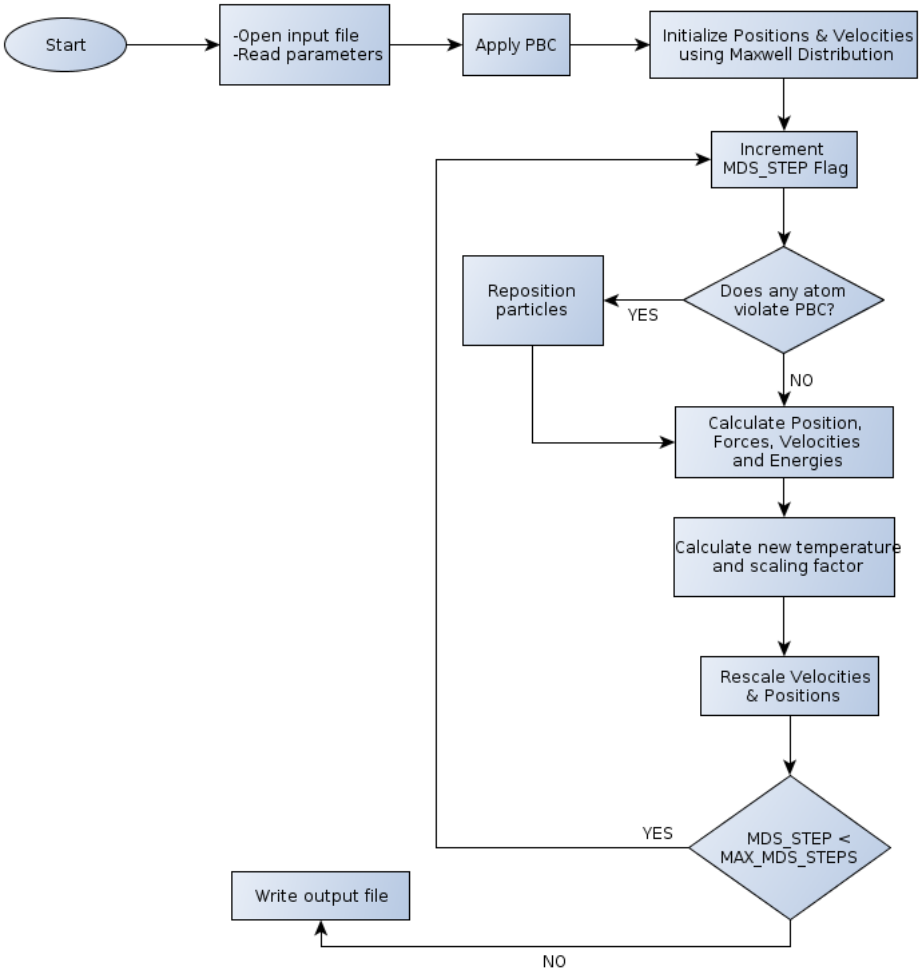

Figure C.1: Flow Chart of the molecular dynamics simulation (MDS) program used in the current study.